

CORRELATION BETWEEN X-RAY AND RADIO ABSORPTION IN COMPACT RADIO GALAXIES

LUISA OSTORERO^{1,2}, RAFFAELLA MORGANTI^{3,4}, ANTONALDO DIAFERIO^{1,2}, ANETA SIEMIGINOWSKA⁵,
ŁUKASZ STAWARZ⁶, RAFAL MODERSKI⁷, AND ALVARO LABIANO⁸

Draft version October 18, 2018

ABSTRACT

Compact radio galaxies with a GHz-peaked spectrum (GPS) and/or compact-symmetric-object (CSO) morphology (GPS/CSOs) are increasingly detected in the X-ray domain. Their radio and X-ray emissions are affected by significant absorption. However, the locations of the X-ray and radio absorbers are still debated. We investigated the relationship between the column densities of the total (N_{H}) and neutral (N_{HI}) hydrogen to statistically constrain the picture. We compiled a sample of GPS/CSOs including both literature data and new radio data that we acquired with the Westerbork Synthesis Radio Telescope for sources whose X-ray emission was either established or under investigation. In this sample, we compared the X-ray and radio hydrogen column densities, and found that N_{H} and N_{HI} display a significant positive correlation, with $N_{\text{HI}} \propto N_{\text{H}}^b$, where $b = 0.47$ and $b = 0.35$, depending on the subsample. The $N_{\text{H}} - N_{\text{HI}}$ correlation suggests that the X-ray and radio absorbers are either co-spatial or different components of a continuous structure. The correlation displays a large intrinsic spread that we suggest to originate from fluctuations, around a mean value, of the ratio between the spin temperature and the covering factor of the radio absorber, $T_{\text{s}}/C_{\text{f}}$.

Keywords: galaxies: active – galaxies: ISM – galaxies: jets – radio lines: ISM – radio lines: galaxies – X-rays: galaxies

1. INTRODUCTION

Compact radio galaxies are a class of radio sources whose radio structure is fully contained within the host galaxy. The most compact ones are well sampled by GHz-peaked spectrum (GPS) galaxies and Compact Symmetric Object (CSO) galaxies, two classes of sub-kpc scale radio galaxies that largely overlap; the former class is characterized by a spectral turnover observed at frequencies about 0.5 – 10 GHz, whereas the latter displays a symmetric radio structure whose emission is most often dominated by two mini-lobes. According to the widely accepted *youth scenario*, GPS/CSO galaxies represent the youngest fraction of the radio galaxy population ($< 10^4$ years): they would first evolve into the larger, sub-galactic scale compact steep spectrum sources with medium symmetric object morphology (CSS/MSOs), and then possibly further expand beyond their host galaxy, becoming large-scale radio sources (Fanti et al. 1995; Readhead et al. 1996; Snellen et al. 2000). However, intermittency of the central engine (Reynolds & Begelman 1997; Czerny et al. 2009) and possible slowing down or disruption of the jet flow (Alexander 2000; Wagner et al. 2012; Perucho 2016, and references therein) may play an important role in this evolu-

tionary path. Regardless of whether they are newly born or restarted sources, GPS/CSOs are ideal laboratories to investigate the interplay between the active galactic nucleus (AGN) and the interstellar medium (ISM) in the early phase of the jet activity.

Although still relatively small, the sample of X-ray detected compact radio galaxies is steadily increasing. Among them, GPS/CSOs have displayed a very high detection rate ($\sim 100\%$) in a number of X-ray studies during the last decades (O’Dea et al. 2000; Risaliti et al. 2003; Guainazzi et al. 2004, 2006; Vink et al. 2006; Siemiginowska et al. 2008; Tengstrand et al. 2009; Siemiginowska et al. 2016); one of them was recently detected also in the γ -ray domain (Migliori et al. 2016). The best angular resolution currently available in the X-ray band ($\sim 1''$ with *Chandra*) is not sufficient to resolve the X-ray morphology of most GPS/CSOs. Extended emission has been detected only in two sources, PKS 1345+125 (Siemiginowska et al. 2008) and PKS 1718–649 (Siemiginowska et al. 2016); therefore, both the nature and the production site of the observed X-rays have been mostly investigated through X-ray spectral studies, and are still highly model dependent. X-rays in GPS/CSOs have been proposed to be thermal emission from the ISM shocked by the expanding radio lobes (Heinz et al. 1998; O’Dea et al. 2000), thermal Comptonization emission from the disc corona (Guainazzi et al. 2004; Vink et al. 2006; Guainazzi et al. 2006; Siemiginowska et al. 2008, 2016; Tengstrand et al. 2009), or non-thermal emission of compact lobes produced through inverse-Compton scattering of the local radiation fields (Stawarz et al. 2008; Ostorero et al. 2010; Siemiginowska et al. 2016). All these thermal and non-thermal components are, in fact, likely to contribute to the total X-ray emission of compact radio galaxies, but they are difficult to disentangle (Siemiginowska 2009; Siemiginowska et al. 2016; Tengstrand et al. 2009).

Both radio and X-ray emissions often appear to be affected by significant absorption within the sources, and the absorbers

Electronic address: ostorero@ph.unito.it

¹ Dipartimento di Fisica, Università degli Studi di Torino, Via P. Giuria 1, I-10125 Torino, Italy

² Istituto Nazionale di Fisica Nucleare (INFN), Sezione di Torino, Via P. Giuria 1, I-10125 Torino, Italy

³ Netherlands Institute for Radio Astronomy, Postbus 2, 7990 AA Dwingeloo, The Netherlands

⁴ Kapteyn Astronomical Institute, University of Groningen, P.O. Box 800, 9700 AV Groningen, The Netherlands

⁵ Harvard-Smithsonian Center for Astrophysics, 60 Garden St., Cambridge, MA 02138, USA

⁶ Astronomical Observatory, Jagiellonian University, ul. Orla 171, 30-244 Kraków, Poland

⁷ Nicolaus Copernicus Astronomical Center, Bartycka 18, 00-716 Warsaw, Poland

⁸ Institute for Astronomy, Department of Physics, ETH Zurich, CH-8093 Zurich, Switzerland

may be characterized by complex structures and geometries, as detailed in Section 2. The neutral hydrogen column density of the radio absorber, N_{HI} , can be estimated from HI absorption measurements, and the total hydrogen equivalent column density of the X-ray absorber, N_{H} , can be derived from X-ray spectral studies.

The comparisons presented in the literature between N_{H} and N_{HI} in GPS/CSOs indicate that the N_{H} values are systematically larger than the N_{HI} values by 1–2 orders of magnitudes (e.g., Vink et al. 2006; Tengstrand et al. 2009). Furthermore, a significant positive correlation between N_{H} and N_{HI} was discovered by Ostorero et al. (2009, 2010): in a sample of 10 GPS/CSOs, they found $N_{\text{H}} \propto N_{\text{HI}}^\alpha$, where $\alpha \simeq 1$. This correlation is indeed expected if the radio and X-ray absorbers are physically connected and the physical and geometrical properties of the absorbers are comparable in different GPS/CSOs. Conversely, no correlation is expected if the two absorbers are not physically connected. Therefore, the possible relationship between N_{H} and N_{HI} deserves to be carefully investigated.

Motivated by this finding, and with the aim of investigating the $N_{\text{H}} - N_{\text{HI}}$ relationship for the whole sample of GPS/CSOs known to be X-ray emitters, we carried out a program of observations with the Westerbork Synthesis Radio Telescope (WSRT) aimed at searching for HI absorption in the GPS/CSOs still lacking an HI detection. Preliminary results of this project were presented in Ostorero et al. (2016).

The paper is organized as follows: in Section 2, we present the main physical and observational aspects of the X-ray and HI absorption measurements. In Section 3, we present the observations and data analysis of the source sample that we observed with the WSRT. In Section 4, we review the source sample that is the subject of our $N_{\text{H}} - N_{\text{HI}}$ investigation. In Sections 5 we present the correlation analysis. We discuss our results in Section 6, and we draw our conclusions in Section 7.

2. PHYSICAL AND OBSERVATIONAL ASPECTS OF THE ABSORPTION

In the radio band, observations of the spin-flip transition of neutral atomic hydrogen (HI) in absorption, at the rest-frame frequency of 1.420 GHz ($\lambda=21$ cm),⁹ are a powerful tool to probe the neutral, atomic ISM. Several HI absorption surveys revealed that compact radio galaxies display a significant excess in the detection rate with respect to extended radio sources (Conway 1997; Morganti et al. 2001; Pihlström et al. 2003; Vermeulen et al. 2003; Gupta et al. 2006; Chandola et al. 2011; Curran et al. 2013; Geréb et al. 2014).

In particular, Curran et al. (2013) were able to associate this excess with compact sources characterized by projected linear sizes of 0.1–1 kpc (detected with a rate $\gtrsim 50\%$, compared to a rate $\lesssim 30\%$ for sources with either smaller or larger sizes). This finding may indicate that the typical cross-section of cold, absorbing gas is 0.1–1 kpc, in “resonance” with the radio source size. The detection rate of HI absorption was also found to be partly affected by the UV luminosity of the AGN: in sources with $L_{\text{UV}} > 10^{23}$ W Hz⁻¹, mostly extended, a larger fraction of the hydrogen reservoir may be ionized, decreasing the likelihood of HI detection (Curran & Whiting 2010; Allison et al. 2012). The statistics of HI detections thus seem to suggest that compact radio sources are hosted by systems that are, on average, richer in

neutral gas than extended sources and that this gas is mostly concentrated in structures with typical linear size of 0.1–1 kpc, i.e., larger than the pc-scale dusty tori required by unification schemes (Antonucci 1993; Urry & Padovani 1995; Tadhunter 2008) and recently imaged in nearby Seyfert galaxies (e.g., Jaffe et al. 2004; Raban et al. 2009; Tristram et al. 2009, 2014).

Absorbers with a size of 0.1–1 kpc were also shown to best account for the anticorrelation between the peak observed optical depth, $\tau_{\text{obs,peak}}$, and the projected linear size of radio sources (Curran et al. 2013): for a given intrinsic optical depth, τ , this anticorrelation arises from the proportionality between $\tau_{\text{obs,peak}}$ and the fraction of the source covered by the absorber (i.e., the covering factor, C_{f}), and is thus a mere consequence of geometry. This anticorrelation also drives the anticorrelation between HI column density, N_{HI} , and projected linear size discovered by Pihlström et al. (2003) for compact radio sources.

However, the actual geometry and dynamical state of the absorbing gas are still a matter of debate. HI absorption spectra of compact sources reveal not only a wide range of observed optical depths ($\tau_{\text{obs,peak}} \sim 0.001\text{--}0.9$), but also a remarkable variety of line profiles (Gaussian, multi-peaked, irregular). These profiles are characterized (i) by widths spanning from less than 10 km s⁻¹ to more than ~ 1000 km s⁻¹ (with typical values of 100–200 km s⁻¹), and (ii) by spectral velocities either coincident with the systemic velocity of the galaxy or red/blue-shifted up to ~ 1000 km s⁻¹. Prominent red or blue wings spanning several 100 km s⁻¹ are also detected in some sources (e.g., Vermeulen et al. 2003; Morganti et al. 2003, 2004; Glowacki et al. 2017). All this evidence suggests that the kinematics of the absorbing gas can be complex. Specifically, as shown by Geréb et al. (2014, 2015) and by Glowacki et al. (2017), the tendency of compact sources to have broader, deeper, more asymmetric, and more commonly blue-/red-shifted absorption line profiles than extended sources likely reflects the presence of unsettled gas distributions, possibly generated by the interaction of the expanding jets with the circumnuclear medium. On the other hand, a fraction of compact sources seems to be depleted of cold atomic gas, as revealed by stacking techniques applied to the spectra of non-detected sources (Geréb et al. 2014); the nature of this dichotomy is not clear yet.

In the limited sample of compact sources with available high angular resolution HI absorption measurements, the HI is typically detected against one or both radio lobes (Araya et al. 2010; Morganti et al. 2013, and references therein), although not against the radio core (see, however, Peck & Taylor 2001). On the other hand, the core is often very weak or undetected at frequencies of 5 GHz or higher (Taylor et al. 1996; Araya et al. 2010). The estimated HI covering factors, C_{f} , vary from ~ 0.2 (Morganti et al. 2004, 2013) to ~ 1 (Peck et al. 1999). The general consensus is that the absorber has an inhomogeneous or clumpy structure, although the actual distribution of the gas is not known. The proposed scenarios include circumnuclear, clumpy tori (e.g., Peck & Taylor 2001) and inclined, thin, clumpy discs (e.g., Araya et al. 2010) with sizes of ~ 100 pc, and/or clouds interacting with the expanding jets and lobes (Morganti et al. 2004, 2013), falling toward the nucleus (Conway 1999), or located in a kpc-scale galactic disc (Perlman et al. 2002) that might be randomly oriented with respect to the pc-scale torus (Curran et al. 2008; Emonts et al. 2012). Evidence of circumnuclear atomic discs with sizes of ~ 100 pc and/or infalling

⁹ This process is usually referred to as associated absorption.

clouds was also found in the central regions of extended radio galaxies, including Centaurus A (Morganti et al. 2008) and Cygnus A (Struve & Conway 2010).

In the X-ray band, the spectra of GPS/CSOs reveal a significant, although moderate, degree of intrinsic absorption. Tengstrand et al. (2009) found that the mean column density value of their GPS/CSO sample, $N_{\text{H}} = 3 \times 10^{22} \text{ cm}^{-2}$ ($\sigma_{N_{\text{H}}} \simeq 0.5$ dex), is much higher than that of a control sample of extended radio galaxies of the FR-I type ($N_{\text{H}} = 3.3_{-0.7}^{+2.1} \times 10^{21} \text{ cm}^{-2}$), whose core emission does not appear to be obscured by dusty tori (Chiaberge et al. 1999; Donato et al. 2004), and is intermediate between the values of unobscured ($N_{\text{H}} \lesssim 10^{22} \text{ cm}^{-2}$) and highly obscured ($N_{\text{H}} \gtrsim 10^{23} \text{ cm}^{-2}$) FR-II radio galaxies, where the presence of optically thick tori is supported by optical and X-ray observations (Sambruna et al. 1999; Chiaberge et al. 2000). On the other hand, in the CSO sample analyzed by Siemiginowska et al. (2016), there appears to be an overabundance ($\sim 60\%$) of sources with mild intrinsic obscuration, $N_{\text{H}} < 10^{22} \text{ cm}^{-2}$. The mean column density of the full sample is $N_{\text{H}} \simeq (2-4) \times 10^{21} \text{ cm}^{-2}$ ($\sigma_{N_{\text{H}}} \simeq 0.3$ dex), depending on whether only detections or both detections and upper limits are taken into account; these values are consistent with the hydrogen column densities of FR-I and unobscured FR-II radio galaxies that we mentioned above.

The geometry and scales of the X-ray obscuring circumnuclear structures in AGN are still debated: the ratio between Type-2 and Type-1 AGN requires a geometrically thick torus, that is modeled in different ways, e.g. as a pc-scale, dusty donut (e.g., Krolik & Begelman 1988), or as a dust-free, sub-pc scale, clumpy outflow closely related to the broad-line emission region (Risaliti et al. 2007, 2010, 2011; Nenkova et al. 2008). Whether or not the X-ray obscuration of GPS/CSOs fits any of these scenarios is not clear, and any relationship between the radio and X-ray absorbers may help to clarify the picture.

As mentioned in Section 1, the neutral hydrogen column densities, N_{HI} , appear to be systematically lower than the total hydrogen equivalent column densities, N_{H} , by 1–2 orders of magnitudes, in GPS/CSOs for which both X-ray and spatially unresolved HI spectra are available (e.g., Vink et al. 2006; Tengstrand et al. 2009). This discrepancy may indicate that the X-ray and radio measurements trace different absorbers, in agreement with a scenario where the X-rays originate in the accretion-disc corona, and are consequently more affected by obscuration than the radio waves with $\lambda = 21$ cm produced farther from the AGN (e.g., Vink et al. 2006; Tengstrand et al. 2009). However, care should be taken when comparing the radio and X-ray hydrogen column densities.

First, the estimate of N_{HI} depends on the ratio between the spin temperature of the absorbing gas and the covering factor, $T_{\text{s}}/C_{\text{f}}$ (e.g. Wolfe & Burbidge 1975; O’Dea et al. 1994; Gallimore et al. 1999), a parameter that is often poorly constrained; common assumptions are $T_{\text{s}} = 100$ K and $C_{\text{f}} = 1$, suitable for a cold gas cloud in thermal equilibrium, and thus with the spin temperature equal to the kinetic temperature ($T_{\text{s}} = T_{\text{k}}$), that fully covers the radio source. Secondly, the HI absorption measurements trace the content of the absorbing system in terms of neutral hydrogen (N_{HI}), whereas the X-ray spectral measurements enable to constrain, for a given X-ray emission model, the content of total (i.e., neutral, molecular, and ionized) hydrogen ($N_{\text{H}} = N_{\text{HI}} + N_{\text{H}_2} + N_{\text{HII}}$) in an absorber with a given ele-

mental abundance (e.g., Wilms et al. 2000); full coverage of the X-ray source by the absorber is also typically assumed. A difference between N_{HI} and N_{H} is thus expected in a single absorbing system composed of gas that is not fully atomic and neutral; this difference is ultimately set by the temperature of the gas (e.g., Maloney et al. 1996).

When the absorber is cold, and the assumption $T_{\text{k}} = T_{\text{s}} = 100$ K is reasonable for the HI gas, the abundance of molecular hydrogen may be high (e.g., Maloney et al. 1996) and may partly account for the $N_{\text{H}} - N_{\text{HI}}$ discrepancy. On the other hand, when the neutral hydrogen is warmer than typically assumed, with $T_{\text{s}} \simeq \text{few } 10^3$ K, as expected in the circumnuclear AGN environment (Bahcall & Ekers 1969; Maloney et al. 1996; Liszt 2001), the N_{HI} estimated from the observed optical depth τ_{obs} increases accordingly, and may become comparable to the N_{H} estimates.

The assumption of a partial coverage of the source by the absorber ($C_{\text{f}} < 1$) affects both the N_{HI} and the N_{H} estimates, but the details of this effect are still to be investigated.

Despite the above uncertainties, which affect the magnitude of the $N_{\text{H}} - N_{\text{HI}}$ offset, the existence of a correlation between N_{H} and N_{HI} (Ostorero et al. 2010, 2016), which we confirm below, clearly points toward a physical connection between the X-ray and radio absorbers.

3. HI OBSERVATIONS AND DATA ANALYSIS

3.1. Target sample

A summary of our observing program with the WSRT is reported in Table 1. We searched for HI absorption in a sample of 12 GPS/CSOs, hereafter referred to as the *target sample*, drawn from a larger sample of X-ray emitting GPS/CSOs described in Section 4. The target sources are listed in Table 1, Column 1 (and are also marked with an asterisk in the last column of Table 5). Their optical redshifts are reported in Column 2 of the same Table.

Four out of twelve targets (i.e., 0035+227, 0026+346, 2008–068, and 2128+048) were not searched for HI absorption prior to our study. In the remaining eight targets, HI absorption was not detected in previous observations, and upper limits to the HI optical depth could be estimated for five of them (see Table 5). We observed these eight sources again to either improve the available upper limits or attempt the first estimate of their HI optical depths.

3.2. Observations

The setup of the observations is summarized in Table 1, Columns 3–6.

The observations were carried out with the WSRT in five observing runs from 2008 to 2011. The target sources were observed either with the UHF-high-band receiver (appropriate when $z \gtrsim 0.2$) or with the L-band receiver (appropriate when $z < 0.2$), in dual orthogonal polarization mode. Each target was observed for an exposure time of 3.5–12 hours. The observing band was either 10 or 20 MHz wide, with 1024 spectral channels, and was centered at the frequency ν_{obs} where the HI absorption line is expected to occur, based on the spectroscopical optical redshift. Compared to the HI survey of compact sources by Vermeulen et al. (2003), where a 10 MHz wide band and 128 spectral channels were available, our observations could benefit from a larger ratio between number of spectral channels and observing bandwidth; this improvement, together with the longer exposure times, had the potential to enable a more effective separation of narrow HI absorption features from radio frequency interferences (RFI).

However, in many cases, we were forced to adopt a 10 MHz wide band in order to minimize the in-band effect of nearby RFI.¹⁰ The 10 MHz bandwidth enabled us to cover a velocity range about the velocity centroid of approximately ± 1200 km s⁻¹ at $z \simeq 0.1$, increasing to approximately ± 2000 km s⁻¹ at $z \simeq 1$. When we could use a 20 MHz wide band, the above velocity ranges increased to approximately ± 2300 km s⁻¹ and ± 4200 km s⁻¹, respectively.

A primary calibrator (either 3C 48, 3C 147 or 3C 286) was observed before and after each target pointing, and used as a flux and bandpass calibrator.

3.3. Data analysis

The integration time of our observations was typically of only a few hours (see Table 1). For an east-west array like the WSRT, this implies that the synthesized beam of the data cubes is very elongated. However, our targets are all unresolved by the WSRT; therefore, this is not an issue for the results presented in this work.

The data were calibrated and reduced using the MIRIAD package (Sault et al. 1995). The continuum subtraction was done by performing a linear fit of the spectrum through the line-free channels of each visibility record, and subtracting the fitting function from all the frequency channels (“UVLIN”). The spectral-line cube was obtained by averaging a few (typically three or four) channels together and adopting uniform weighting. The data were Hanning smoothed to suppress the Gibbs ripples. The final velocity resolution of the data cubes, together with the 3σ rms noise, are listed in Table 1, Columns 7 and 8.

For all but one target source, we used the UHF-high-band receiver: this receiver, unlike the L-band receiver, is uncooled. Therefore, despite the technical improvements described in Section 3.2, our observations were affected by a relatively high noise level.

3.4. HI results

We detected HI absorption in 2 out of 12 targets, 0035+227 and 0941–080. For seven targets, we could estimate upper limits to the optical depth of a putative HI absorption line. However, in three cases, the quality of our observations turned out to be lower than the quality of the observations previously performed by Vermeulen et al. (2003). This appears to be due to degradation of the band caused by extra RFI. In these three cases, we used the constraints on the optical depth derived by Vermeulen et al. (2003) for our correlation analysis (see Section 5). For the remaining three targets, located at redshift $z = 0.517 - 0.547$, the RFI were too strong to obtain any useful data, despite the above technical improvements.

For the sources in which we detected HI absorption, the peak optical depth, $\tau_{\text{obs,peak}}$, the line width, ΔV (corresponding to the full width at half maximum), and the peak velocity, $v_{\text{obs,peak}}$, were determined through Gaussian fitting of the absorption profiles. For the sources in which no HI absorption was detected, 3σ upper limits to τ_{peak} were estimated from the continuum flux density and the rms noise level of the spectra. The estimates of $\tau_{\text{obs,peak}}$, ΔV , and v_{peak} are reported in Table 1, Columns 11, 12, and 13, respectively. The flux density of the continuum and, for the detections only, its difference from the flux density of the line peak are given in Columns 9 and 10, respectively.

¹⁰ The frequencies corresponding to the redshifts of these sources are close to the GSM band and bands allocated to TV broadcast.

The atomic hydrogen column density along the line of sight (in units of cm⁻²) is related to the velocity-integrated optical depth of the HI absorption profile through the following relationship (e.g., Wolfe & Burbidge 1975; O’Dea et al. 1994; Curran et al. 2013):

$$N_{\text{HI}} = 1.823 \times 10^{18} T_s \int \tau(v) dv, \quad (1)$$

where T_s is the spin temperature in K, v is the velocity in units of km s⁻¹, and the optical depth is given by

$$\tau(v) = -\ln \left[1 - \frac{\tau_{\text{obs}}(v)}{C_f} \right]. \quad (2)$$

Here, the observed optical depth, $\tau_{\text{obs}}(v)$, is the ratio between the spectral line depth in a given velocity channel and the continuum flux density of the background radio source: $\tau_{\text{obs}}(v) \equiv \Delta S(v)/S_{\text{cont}}(v) = (S(v) - S_{\text{cont}}(v))/S_{\text{cont}}(v)$.

In the optically thin regime (i.e., for $\tau \lesssim 0.3$), the observed optical depth of the line is related to the actual optical depth through $\tau(v) \approx \tau_{\text{obs}}(v)/C_f$, and Equation (1) can be approximated by

$$N_{\text{HI}} \approx 1.823 \times 10^{18} (T_s/C_f) \int \tau_{\text{obs}}(v) dv. \quad (3)$$

Therefore, the HI column density can be derived from the integrated observed optical depth, $\tau_{\text{obs}} \equiv \int \tau_{\text{obs}}(v) dv$, once the ratio T_s/C_f is known.

We computed the HI column densities (in cm⁻²) of the detected sources from Equation (3), with $\tau_{\text{obs}}(v)$ replaced by its Gaussian fitting function. For consistency with the literature, we estimated N_{HI} by assuming that the absorber fully covers the radio source ($C_f=1$), and that the spin temperature of the absorbing gas is $T_s=100$ K. These assumptions yield N_{HI} values that likely represent lower limits to the actual column densities (see Section 2).

When we did not detect any HI line, we used the following equation to estimate 3σ upper limits to N_{HI} from the 3σ upper limits to the observed optical depth, $\tau_{\text{obs},3\sigma}$:

$$N_{\text{HI},3\sigma} = 1.823 \times 10^{18} (T_s/C_f) \tau_{\text{obs},3\sigma} \Delta V, \quad (4)$$

under the assumption that the putative absorption line has $\Delta V = 100$ km s⁻¹ (Vermeulen et al. 2003). Our estimates of N_{HI} are reported in Table 1, Column 14.

3.4.1. HI absorption in 0035+227

Our spectrum of source 0035+227 is displayed in Figure 1. We detected one absorption feature with a complex profile. A Gaussian fit to the optical depth velocity profile yields a peak optical depth $\tau_{\text{obs,peak}} = 0.0181 \pm 0.0014$, a line width $\Delta V = (114 \pm 10)$ km s⁻¹, and a peak velocity $v_{\text{peak}} = (29197 \pm 4)$ km s⁻¹. The systemic velocity of the host galaxy, derived from its heliocentric redshift, $z = 0.096 \pm 0.002$, estimated by Marcha et al. (1996) from an optical spectrum of the source, is $v_{\text{sys}} = (28780 \pm 600)$ km s⁻¹. The peak velocity of the absorption line is consistent with the systemic velocity of the galaxy at 1σ confidence level. We derived an HI column density $N_{\text{HI}} = (3.99 \pm 0.49) \times 10^{20}$ cm⁻² for the gas responsible for the absorption line, under the assumption that $C_f = 1$ and $T_s = 100$ K.

Table 1
 WSRT Observations: Source Sample, Observation Details, Results of the Data Analysis,
 and Estimates of the HI Column Density.

Source Name	$z_{\text{opt}}^{\text{a}}$	Receiver	t_{exp}	Bandwidth	ν_{obs}	Spectral Res.	rms	S_{cont}	$S_{\text{cont}} - S_{\text{HI,peak}}$	$\tau_{\text{obs,peak}}$	ΔV	v_{peak}	N_{HI}
B1950	(2)	(3)	(h)	(MHz)	(MHz)	(km s^{-1})	(mJy/b)	(Jy)	(mJy)	(10^{-2})	(km s^{-1})	(km s^{-1})	($10^{20} \frac{N_{\text{HI}}}{100 \text{ K}} \text{ cm}^{-2}$)
(1)	(2)	(3)	(4)	(5)	(6)	(7)	(8)	(9)	(10)	(11)	(12)	(13)	(14)
0019–000	0.305	UHF-high	5	10	1088	16	7.8	2.8	...	< 0.84	< 1.5 ^{b,c}
0026+346	0.517	UHF-high	4	10	936.3
0035+227	0.096±0.002	L-band	4	20	1296	20	1.5	0.583	11	1.81 ± 0.14	114 ± 10	29,197 ± 4	3.99 ± 0.49
0710+439	0.518	UHF-high	4	10	935.7
0941–080	0.2281±0.0013 ^d	UHF-high	5	10	1156.7	8	1.7	2.58	7	0.22 ± 0.02	215 ± 18	68,156 ± 8	0.91 ± 0.10
1031+567	0.459 ^e	UHF-high	3.5	20	973.6	34	6.6	1.99	...	< 0.99	< 1.8 ^{b,c}
1117+146	0.362	UHF-high	5	10	1043	16	5.6	2.7	...	< 0.62	< 1.1 ^{b,c}
1607+268	0.473	UHF-high	5	10	964	16	14	4.88	...	< 0.86	< 1.6 ^{b,c}
1843+356	0.764	UHF-high	12	20	805.2	16	5.3	0.248	...	< 6.41	< 11.7 ^{b,c}
2008–068	0.547	UHF-high	5	10	918.2
2021+614	0.227	UHF-high	4	20	1157.6	16	0.98	1.99	...	< 0.15	< 0.27 ^{b,c}
2128+048	0.99	UHF-high	8	10	713	8	17	4.46	...	< 1.14	< 2.08 ^{b,d}

^a Redshift uncertainties are reported only for the sources in which HI absorption was detected, for comparison with the HI absorption line peak velocity.

^b 3σ upper limit.

^c From results on $\tau_{\text{obs},3\sigma}$, using the relation: $N_{\text{HI},3\sigma} = 1.823 \times 10^{18} \times T_{\text{s}} \times \tau_{\text{obs},3\sigma} \times \Delta V$, under the assumptions $T_{\text{s}}=100 \text{ K}$, $\Delta V = 100 \text{ km s}^{-1}$, and $C_f = 1$.

^d W.H. de Vries, private communication.

^e In a previous paper (Ostorero et al. 2016), we used the redshift value $z = 0.45$ (Pearson & Readhead 1988) for this source. This redshift is incorrect, and was here replaced by the more appropriate value $z = 0.4590 \pm 0.0001$ (Dunlop et al. 1989).

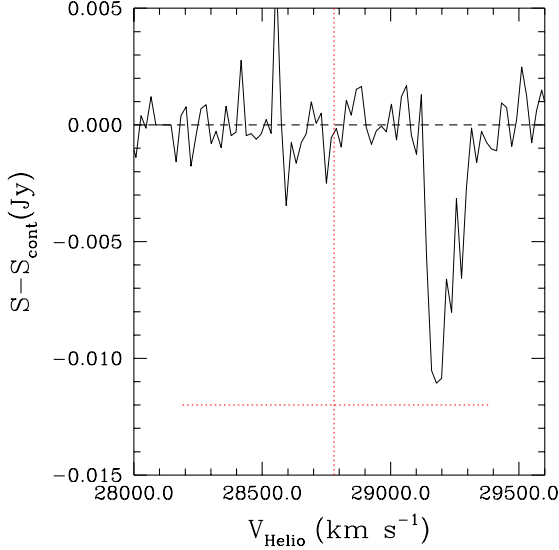


Figure 1. Spectrum of the CSO 0035+227, with velocities displayed in the optical heliocentric convention. The systemic velocity of the optical galaxy is $v_{\text{sys}} = (28,780 \pm 600) \text{ km s}^{-1}$: v_{sys} is marked with a vertical, dotted line; the horizontal, dotted line shows its 1σ uncertainty. A complex absorption line, with $\tau_{\text{obs,peak}} = 0.0181 \pm 0.0014$ and $\Delta V = (114 \pm 10) \text{ km s}^{-1}$, is detected about v_{sys} .

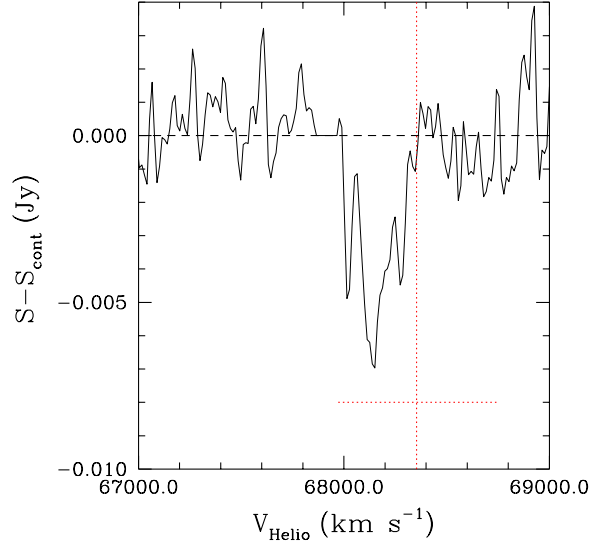


Figure 2. Spectrum of the GPS/CSO galaxy 0941–080, with velocities displayed in the optical heliocentric convention. The systemic velocity of the optical galaxy is $v_{\text{sys}} = (68,353 \pm 390) \text{ km s}^{-1}$: v_{sys} is marked with a vertical, dotted line; the horizontal, dotted line shows its 1σ uncertainty. A broad, multi-peaked absorption feature with $\tau_{\text{obs,peak}} = 0.0022 \pm 0.0002$ and $\Delta V = (215 \pm 18) \text{ km s}^{-1}$ is detected about v_{sys} .

3.4.2. HI absorption in 0941–080

In the spectrum of 0941–080, shown in Figure 2, we detected a broad, multi-peaked absorption feature. A Gaussian fit to the optical depth velocity profile yields a peak optical depth $\tau_{\text{obs,peak}} = 0.0022 \pm 0.0002$, a line width $\Delta V = (215 \pm 18) \text{ km s}^{-1}$, and a peak velocity $v_{\text{peak}} = (68156 \pm 8) \text{ km s}^{-1}$. The systemic velocity of the host galaxy, derived from the heliocentric redshift estimated from the optical spectrum of the source, $z = 0.2281 \pm 0.0013$ (de Vries et al. 2000, de Vries, private communication), is $v_{\text{sys}} = (68353 \pm 390) \text{ km s}^{-1}$. The peak velocity of the absorption line is consistent with the systemic velocity of the galaxy at 1σ confidence level. For the gas responsible for this associated absorption, we derived an HI column density $N_{\text{HI}} = (9.1 \pm 1.0) \times 10^{19} \text{ cm}^{-2}$, under the assumption that $C_f = 1$ and $T_s = 100 \text{ K}$. This detection of HI absorption in the source is the first ever, and it was enabled by the improved observation setup (see Section 3.2). Previous observations (Vermeulen et al. 2003) could only set upper limits to the optical depth of a putative absorption line (see Table 5). The optical depth that we measured is consistent with the previously estimated upper limits.

4. $N_{\text{H}} - N_{\text{HI}}$ SAMPLE DEFINITION

By using our own data and those from the literature, we compiled the largest sample of GPS/CSOs that were targets of both X-ray and HI-absorption observations. The GPS/CSOs observed in the X-rays were all detected in this band, and they constitute a subsample of the GPS/CSOs observed in the HI band: therefore, the sample that we compiled consists of all the X-ray detected GPS/CSOs that were also observed in the HI band, i.e. 27 compact radio galaxies. This sample includes sources that were investigated in the X-ray band, either individually or in small samples, by different authors and with different instruments; it can be considered as the merger of two, partly overlapping, subsamples of sources

that were selected for X-ray investigations with different criteria. The first subsample is a flux- and volume-limited sample of 17 GPS galaxies, with $F_{5 \text{ GHz}} > 1 \text{ Jy}$ and $z < 1$, extracted by Tengstrand et al. (2009) and Guainazzi et al. (2006) from the complete sample of GPS sources compiled by Stanghellini et al. (1998); these GPS galaxies are located at redshift $z = 0.0773 - 0.99$, and have radio luminosities at $\nu = 1.4 \text{ GHz}$ spanning the range $L_{1.4 \text{ GHz}} = 10^{25} - 10^{28.4} \text{ W Hz}^{-1}$; 16 of them were morphologically classified as CSOs. The second subsample is a sample of 16 CSOs with known redshifts and estimated kinematic ages, compiled by Siemiginowska et al. (2016); these CSOs are located at redshift $z = 0.0142 - 0.764$, and have radio luminosities at $\nu = 1.4 \text{ GHz}$ spanning the range $L_{1.4 \text{ GHz}} = 10^{24} - 10^{27.6} \text{ W Hz}^{-1}$; 15 of them were spectroscopically classified as GPS sources. The two subsamples have six sources in common. Overall, the 27 sources of the full sample are located at redshift $z = 0.0142 - 0.99$, and they have moderate to high radio luminosities, $L_{1.4 \text{ GHz}} = 10^{24} - 10^{28.4} \text{ W Hz}^{-1}$.¹¹ Even though the sample is not complete and well-defined in terms of flux limit and volume, it is the largest sample of GPS/CSOs available to date for which both X-ray and HI observations were carried out. The main properties of the sources of this sample, including all the available HI and X-ray column density estimates, are summarized in Tables 5 and 6.

In order to perform the $N_{\text{H}} - N_{\text{HI}}$ correlation analysis, from the above sample of 27 GPS/CSOs we extracted the subsample of sources for which an estimate of both N_{HI} and N_{H} was available. By “estimate” we mean either a value or an upper/lower limit. The three sources 0026+346, 0710+439, and 2008–068 have no N_{HI} estimate (see Sections 4.1 and Table 5), and the two sources 0116+319 and 1245+676 have no N_{H} estimate (see Sections 4.2 and Table 6). Therefore, we were left with a subsample of 22 sources, that we refer to

¹¹ Only 3 out of 27 sources have $L_{1.4 \text{ GHz}} < 10^{25} \text{ W Hz}^{-1}$: 1245+676, 1509+054, and 1718–649.

hereafter as the *correlation sample*.

The correlation sample spans the redshift range $z = 0.0142 - 0.99$ and the 1.4 GHz luminosity range $L_{1.4 \text{ GHz}} = 10^{24.2} - 10^{28.4} \text{ W Hz}^{-1}$. Table 2 lists the sources of the correlation sample (Column 1), their optical redshifts (Column 2), their radio spectral and morphological classification (Column 3), the estimates of N_{HI} (Column 4) and N_{H} (Column 5) that

we used for the correlation analysis, the type of $(N_{\text{H}}, N_{\text{HI}})$ pair (Column 6), and the sample to which we associated each $(N_{\text{H}}, N_{\text{HI}})$ pair for the correlation analysis (Column 7), as described in Section 4.3. More details on the quantities reported in Table 2 and the criteria that we applied to select the column density estimates given in this table among all the available column density estimates, can be found in the Appendix.

Table 2
Correlation Sample: Column Density Data Set, Pair Types, and Analysis Samples.

Source Name B1950 (1)	z_{opt} (2)	GPS/CSO (3)	N_{HI} ($10^{20} \frac{T_{\text{s}}}{100 \text{ K}} \text{ cm}^{-2}$) (4)	N_{H} (10^{22} cm^{-2}) (5)	Pair Type (6)	Sample ^a (7)
0019-000	0.305	GPS	< 1.5	< 100	UU	E', E''
0035+227	0.096 ± 0.002	CSO	3.99 ± 0.49	$1.4^{+0.8}_{-0.6}$	VV	E', E''
0108+388	0.66847	GPS,CSO	80.5	47.5^{+12}_{-12} ^b	VV	E'
			80.5	> 90 ^c	VL	-
0428+205	0.219	GPS,CSO	3.45^{d}	< 0.69	VU	E', E''
0500+019	0.58457	GPS,CSO	6.2	$0.5^{+0.18}_{-0.16}$	VV	E', E''
0941-080	0.2281 ± 0.0013	GPS,CSO	0.91 ± 0.10	< 1.26	VU	E', E''
1031+567	0.459	GPS,CSO	< 1.26	0.50 ± 0.18	VU	E', E''
1117+146	0.362	GPS,CSO	< 0.63	< 0.16	UU	E', E''
1323+321	0.370	GPS,CSO	0.71	$0.12^{+0.06}_{-0.05}$	VV	E', E''
1345+125	0.12174	GPS,CSO	6.2	4.8 ± 0.4	VV	E', E''
			6.2	$2.543^{+0.636}_{-0.580}$	VV	E', E''
1358+624	0.431	GPS,CSO	1.88	2.9^{+2}_{-1}	VV	E', E''
1404+286	0.07658	GPS,CSO	8.0	$0.13^{+0.12}_{-0.10}$	VV	E'
			8.0	> 90 ^c	VL	-
1509+054	0.084	GPS,CSO	< 3.64	< 0.23	UU	E', E''
1607+268	0.473	GPS,CSO	< 1.6	< 0.18	UU	E', E''
1718-649	0.0142	GPS,CSO	1.477^{d}	0.08 ± 0.07	VV	E', E''
1843+356	0.764	GPS,CSO	< 10.4	$0.8^{+0.9}_{-0.7}$	VU	E', E''
1934-638	0.18129	GPS,CSO	0.06	$0.08^{+0.07}_{-0.06}$	VV	E'
			0.06	> 250 ^c	VL	-
1943+546	0.263	GPS,CSO	4.91	1.1 ± 0.7	VV	E', E''
1946+708	0.101	GPS,CSO	31.6	$1.7^{+0.5}_{-0.4}$	VV	E'
			31.6	> 280 ^c	VL	-
2021+614	0.227	GPS,CSO	< 0.27	< 1.02	UU	E', E''
2128+048	0.99	GPS,CSO	< 2.08	< 1.9	UU	E', E''
2352+495	0.2379	GPS,CSO	2.84^{d}	4^{+7}_{-3}	VV	E', E''

^a The en-dash indicates that the corresponding pair was not included in any sample because it comprises a lower limit (see Section 4.3 for details).

^b This value of N_{H} was estimated as the mean of the 3σ lower limit $N_{\text{H}} > 5 \times 10^{22} \text{ cm}^{-2}$ and the physical upper bound of the Compton-thin N_{H} range, i.e. $N_{\text{H}} > 9 \times 10^{23} \text{ cm}^{-2}$ (see Appendix B and Table 6 for details).

^c This value of N_{H} corresponds to the assumption that the absorber is Compton-thick (see Appendix B and Table 6 for details).

^d Total N_{HI} , estimated as the sum of the N_{HI} values derived from the two absorption lines detected in the spectrum (see Appendix A, Table 5).

4.1. N_{HI} estimates

Detections of HI absorption features, and their corresponding N_{HI} values, were available for 14 out of the 22 sources of the correlation sample; N_{HI} upper limits could be estimated for the remaining eight sources.

We only used N_{HI} estimates derived from low angular resolution measurements, i.e. from measurements that were not able to spatially resolve the source; all our upper limits to N_{HI} are 3σ limits. As mentioned in Sections 2 and 3.4, the N_{HI} estimates depend on the value assumed for the ratio $T_{\text{s}}/C_{\text{f}}$. When an N_{HI} value drawn from the literature was estimated by the authors by assuming $T_{\text{s}}/C_{\text{f}} > 100 \text{ K}$ (i.e.,

$T_{\text{s}} > 100 \text{ K}$ and $C_{\text{f}} = 1$), we rescaled it to an N_{HI} value computed with $T_{\text{s}}/C_{\text{f}} = 100 \text{ K}$. For the 12 sources with more than one N_{HI} estimate, we chose the most suitable estimate, according to the criteria described in Appendix A. The selected N_{HI} estimates are summarized in Table 2, Column 4; they are also listed with the corresponding references in Table 5; we thoroughly comment on these data, as well as on the properties of the full N_{HI} data set, in Appendix A.

4.2. N_{H} estimates

As anticipated in Section 2, the estimate of the column density of the X-ray absorbing gas located at the redshift of the source (i.e., the local absorber) depends on the X-ray emission model adopted to interpret the X-ray spectrum of the source, as well as on the assumed photoionization cross-section of the ISM. For a given abundance of chemical elements in the absorbing gas, the X-ray spectral modeling enables to estimate the equivalent hydrogen column density of the local absorber, N_{H} , i.e., the column density of hydrogen atoms, molecules, and ions toward the source, located at the source redshift (see Appendix B for details).

In the correlation sample, detections of intrinsic X-ray ab-

sorption, and corresponding values of N_{H} , were available for nine out of 22 sources; upper limits to N_{H} were available for eight sources. For the remaining five sources, multiple exposures and ambiguity in the spectral modeling prevented us from selecting a single robust N_{H} value. In particular, for one source, we selected two significantly different N_{H} values corresponding to different observational epochs. For four of them, the ambiguity between a Compton-thin and a Compton-thick absorber in the model adopted for the interpretation of the X-ray spectrum of the source led to the availability of N_{H} estimates lower and greater than $\simeq 10^{24} \text{ cm}^{-2}$, respectively; we considered both scenarios as plausible, and associated with each of these four sources either an N_{H} value (Compton-thin scenario) or a lower limit to N_{H} (Compton-thick scenario).

The N_{H} estimates that we used for our correlation analysis are summarized in Table 2, Column 5; they are also listed with the corresponding references in Table 6; we thoroughly comment on these data, as well as on the properties of the full N_{H} data set, in Appendix B.

4.3. $N_{\text{H}} - N_{\text{HI}}$ sample

The correlation sample consists of 22 sources associated with $(N_{\text{H}}, N_{\text{HI}})$ pairs of estimates of four different types: pairs of *values* (hereafter referred to as *VV* pairs), pairs including a value and an upper limit (*VU* pairs), pairs of upper limits (*UU* pairs), and pairs including a value and a lower limit (*VL* pairs). Specifically, the sample includes four sources unambiguously associated with *VU* pairs, six with *UU* pairs, and eight with *VV* pairs. The sample also includes four sources whose X-ray absorber may be either Compton-thin or Compton-thick (see Section 4.2): each of them is associated with either a *VV* pair or a *VL* pair. The types of $(N_{\text{H}}, N_{\text{HI}})$ pairs associated with the sources of the correlation sample are listed in Table 2, Column 6.

In order to deal with the four ambiguous Compton-thin/Compton-thick sources, we considered two limiting cases in our correlation study. In the first case, we assumed these four sources to be all Compton-thin, and hence we associated them with *VV* pairs. This choice yielded a correlation sample composed of 12 sources with $(N_{\text{H}}, N_{\text{HI}})$ pairs of values (*VV* pairs) and 10 sources with $(N_{\text{H}}, N_{\text{HI}})$ pairs including

upper limits (either *VU* or *UU* pairs), for a total of 22 sources with 23 $(N_{\text{H}}, N_{\text{HI}})$ pairs¹² of estimates of either the *VV*, the *VU*, or *UU* type; hereafter, this sample is referred to as the *estimate sample E'*. The data in sample *E'* have only one type of censoring (i.e., the sample pairs include only values and upper limits; there is no mix of upper and lower limits).

In the second case, we assumed the above four sources to be all Compton-thick, and associated them with the corresponding *VL* pairs. This left us with a correlation sample composed of three main subsamples: a subsample of eight sources with $(N_{\text{H}}, N_{\text{HI}})$ *VV* pairs, a subsample of 10 sources including upper limits (either *VU* or *UU* pairs), and a subsample of four sources including lower limits (*VL* pairs). However, because of difficulties in performing the correlation analysis on samples including data with two types of censoring (i.e., both upper and lower limits; see Section 5 for details), we chose to drop the four *VL* pairs from the correlation sample. The reason why we dropped this subsample of pairs is that this is the smaller of the two subsamples of censored data pairs. Dropping the subsample that includes the *VU* and *UU* pairs would have lowered the total number of sources. Our choice left us with a sample including eight sources with $(N_{\text{H}}, N_{\text{HI}})$ *VV* pairs, and 10 sources with $(N_{\text{H}}, N_{\text{HI}})$ pairs of estimates of either the *VU* or the *UU* type, for a total of 18 sources with 19 $(N_{\text{H}}, N_{\text{HI}})$ pairs of estimates of either the *VV*, the *VU*, or the *UU* type; hereafter, this sample is referred to as the *estimate sample E''*. By construction, the data in sample *E''* have only one type of censoring.

5. CORRELATION ANALYSIS

We performed the correlation analysis on both the estimate samples, *E'* and *E''*, defined in Section 4.3. The results of this analysis are reported in Table 3, and are discussed below. Figure 3 displays the $(N_{\text{H}}, N_{\text{HI}})$ data for these two samples, as well as the corresponding linear regression lines, to guide the eye.

Before discussing these results, we emphasize that correlating N_{H} with N_{HI} is interesting from the point of view of the physics of the sources, although the estimate of N_{HI} is a combination of the measurement of τ_{obs} and the assumption on $T_{\text{s}}/C_{\text{f}}$ ($N_{\text{HI}} \propto \tau_{\text{obs}} \times T_{\text{s}}/C_{\text{f}}$; see Equation 3).

¹² One source is associated with two *VV* pairs; see Section 4.2.

Table 3
Correlation and Regression Analysis for the Estimate Samples, *E'* and *E''*, by means of Survival Analysis Techniques.

Sample ^a	N_{data} (N_{sources})	Generalized Kendall		Generalized Spearman ^d		Schmitt's Linear Regression ^e		Akritas-Theil-Sen Linear Regression	
		z^b	P^c	ρ	P^c	<i>Slope</i> (<i>b</i>)	<i>Intercept</i> (<i>a</i>)	<i>Slope</i> (<i>b</i>)	<i>Intercept</i> (<i>a</i>)
<i>E'</i>	23 (22)	3.044	0.0023	0.679	0.0014	0.820	2.42	0.467	10.3
<i>E''</i>	19 (18)	2.615	0.0089	0.667	0.0046	0.469	10.0	0.345	13.0

^a The samples are defined in Section 4.3 and in Table 2.

^b According to the ASURV Rev. 1.3 software manual, z is an estimated function of the correlation and should not be directly compared to the Spearman's correlation ρ . The values to be compared are the corresponding probabilities.

^c Probability of the null hypothesis of no correlation being true. It is a two-sided significance level: because we are looking a priori for a positive correlation, this value should actually be divided by 2, improving the significance by a factor of 2.

^d According to the ASURV Rev. 1.3 software manual, the generalized Spearman correlation is not dependable for samples with $N < 30$ items, as in our case. In these cases, the generalized Kendall's τ test should be relied upon. We report it here only for comparison purposes.

^e For a bin number of 10 for the data set (see Section 5 for details).

In the estimate samples, we investigated the correlation by means of survival analysis techniques. In particular, we made use of the software package ASURV Rev. 1.3¹³ (LaValley et al. 1992), which implements the methods for bivariate problems presented in Isobe et al. (1986). The gen-

¹³ <http://astrostatistics.psu.edu/statcodes/asurv>

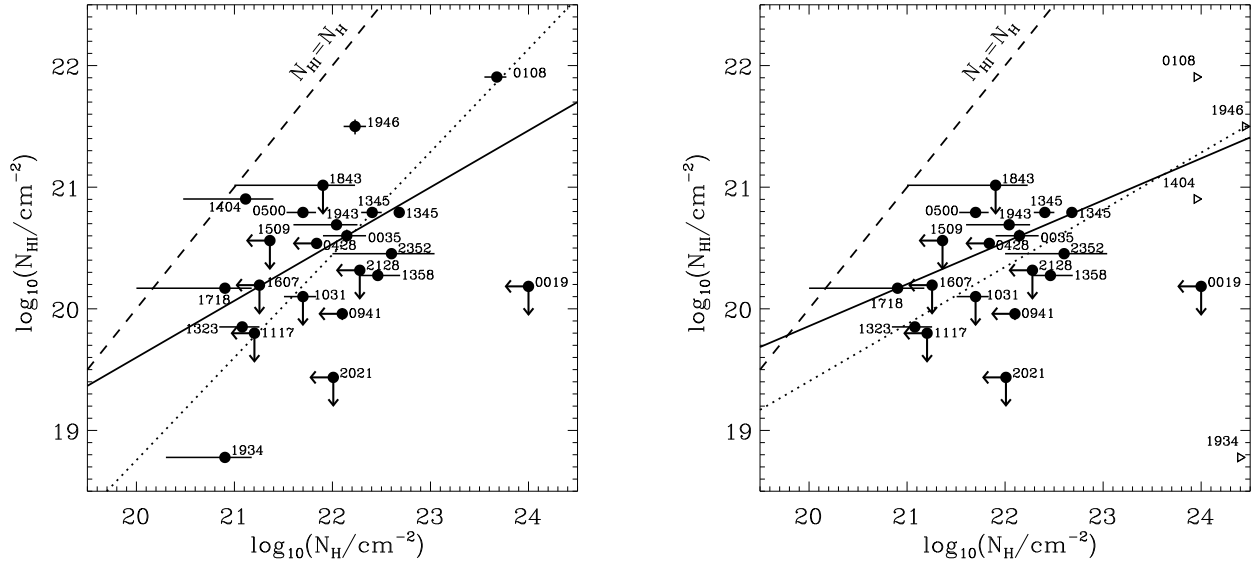


Figure 3. Radio column densities (N_{HI}) as a function of X-ray column densities (N_{H}) for the estimate samples, E' (left) and E'' (right). The solid symbols show the $(N_{\text{H}}, N_{\text{HI}})$ measurements with 1σ error bars on N_{H} . Arrows represent upper limits. Lower limits to N_{H} corresponding to possibly Compton-thick sources are shown in the plot on the right as open triangles, although they were not included in the correlation analysis. Labels show a shortened version of the source names reported in Table 5. N_{HI} was computed by assuming $T_{\text{s}} = 100$ K and $C_{\text{f}} = 1$. Solid line: Akritas-Theil-Sen regression line, to guide the eye ($\log_{10} N_{\text{HI}} = a + b \log_{10} N_{\text{H}}$; see Table 3); dotted line: Schmitt's regression line, for a bin number of 10 (see Section 5 for details); dashed line: bisector of the $N_{\text{H}} - N_{\text{HI}}$ plane.

eralized Kendall's correlation analysis applied to samples E' and E'' shows that the data are significantly correlated: the probability of no correlation being true is $P = 2.3 \times 10^{-3}$ for sample E' , and $P = 8.9 \times 10^{-3}$ for sample E'' . The generalized Spearman's correlation analysis applied to the same samples confirms the above results: $P = 1.4 \times 10^{-3}$ for sample E' , and $P = 4.6 \times 10^{-3}$ for sample E'' . The reason why the significance of the correlation for sample E'' is slightly lower than for sample E' is that sample E'' does not include, among other sources, the two targets characterized by extreme $(N_{\text{H}}, N_{\text{HI}})$ values.

In order to describe the relationship between N_{H} and N_{HI} , we performed a regression analysis with N_{HI} as the dependent variable. The selection criteria of the correlation sample (see Section 4) do not introduce any bias in this sample; therefore, either N_{HI} or N_{H} can formally play the role of the dependent variable. Our choice of N_{HI} as the dependent variable is motivated by the fact that, from a physical perspective, in a given gas distribution, the mass fraction of neutral, atomic gas depends upon the total (i.e., molecular, atomic, and ionized) gas mass through the physical properties of the gas. As a consequence, for the same gaseous structure, the contribution of N_{HI} to N_{H} depends on the physical conditions and on the geometrical distribution of the gas (i.e., temperature and covering factor).

According to the generalized Kendall's and Spearman's tests, we could fit a linear relation to the estimate samples E' and E'' : $\log_{10} N_{\text{HI}} = a + b \log_{10} N_{\text{H}}$. We first performed a linear fit to the data by means of the ASURV Schmitt's linear regression. This method requires a binning of the data set. For sample E' , by varying the number of data bins from 3 to 15, we obtained slopes in the range $b = 0.51 - 0.99$; for sample E'' , by varying the number of data bins from 3 to 15, we obtained slopes in the range $b = 0.41 - 0.57$.

For both E' and E'' , we show the representative results for the case of 10 bins (dotted lines in Figure 3). Because

the results of Schmitt's regression analysis are sensitive to the bin size for small data sets, we performed an additional estimation of the slope with the Akritas-Theil-Sen estimator (e.g., Akritas et al. 1995; Feigelson & Babu 2012), that is implemented in the function *cenken* in the CRAN package NADA within the R statistical software environment. With this method, we found regression-line slopes $b = 0.47$ and $b = 0.35$ for samples E' and E'' , respectively (solid lines in Figure 3). We adopted the slopes derived with the Akritas-Theil-Sen estimator as our trustworthy estimates because of their independence of the binning of the data set.

We note that the Akritas-Theil-Sen method applied to samples E' and E'' after switching the roles of the variables (i.e. by assuming N_{HI} as the independent variable) returned slopes $B = 0.76$ and $B = 1.10$, respectively, for the regression line $\log_{10} N_{\text{H}} = A + B \log_{10} N_{\text{HI}}$, in agreement with our previous results (Ostorero et al. 2009, 2010).

6. DISCUSSION

With the survival analysis methods described in Section 5, we found N_{H} and N_{HI} in samples E' and E'' to be significantly correlated and to be related to each other through the relationship $N_{\text{HI}} \propto N_{\text{H}}^b$, with $b = 0.47$ and $b = 0.35$. Neither the uncertainties on the regression parameters nor the goodness of the fit could be evaluated. However, a visual inspection of this data set suggests a dispersion larger than the typical uncertainties on N_{HI} (see Figure 3).

This fact is supported by the regression analysis of the subsamples that we drew from E' and E'' by selecting the detections only. These two subsamples, hereafter referred to as *detection samples* D' and D'' , respectively, display a significant $N_{\text{H}} - N_{\text{HI}}$ correlation according to both Pearson's and Kendall's correlation analysis. However, the best-fit linear relation turns out not to be a good description of the data ($\chi_{\text{red}}^2 \sim 10$): the dispersion of the data is clearly larger than

the typical uncertainties.¹⁴

This evidence suggests that the observed $N_{\text{H}} - N_{\text{HI}}$ relation is the two-dimensional projection of a multi-dimensional relation, where $T_{\text{s}}/C_{\text{f}}$ is a variable rather than a parameter. In fact, as we show below, $T_{\text{s}}/C_{\text{f}}$ is the most relevant additional variable in the $N_{\text{H}} - N_{\text{HI}}$ relation. There are only two other possible variables; however, they either have a modest impact or, ultimately, depend on T_{s} : (i) the abundance of chemical elements that enters the photoionization cross-section of the X-ray absorbing gas, ultimately affecting the N_{H} estimates in the X-ray spectral fitting; and (ii) the amount of ionized and molecular hydrogen, HII and H_2 .

As for item (i), typical cross-sections adopted in the spectral analysis are based on either solar or ISM abundances. These different assumptions lead to variations of the cross-section by a factor of a few (e.g., Ride & Walker 1977; Wilms et al. 2000), implying corresponding variations of the N_{H} estimates by a factor of a few. This variation is comparable to the average N_{H} uncertainty.

As for item (ii), the abundance of HII and H_2 is an unknown that, in principle, can contribute both to the $N_{\text{H}} - N_{\text{HI}}$ offset and to the spread. This abundance is ultimately set by the kinetic temperature of the gas, T_{k} . If all the sources were characterized by a similar kinetic temperature of the absorber, the fractions of HII and/or H_2 would be comparable in different sources and would only contribute to the offset. On the other hand, if the kinetic temperature were significantly different in different sources, the abundance of HII and H_2 would also contribute to the spread, and N_{H} and N_{HI} might even be uncorrelated in the case of extreme temperature fluctuations. However, we do find a correlation between N_{H} and N_{HI} : we can thus exclude extreme fluctuations in the kinetic temperature, T_{k} .

Similarly, the ratio $T_{\text{s}}/C_{\text{f}}$ might also significantly fluctuate from source to source; for example, it is seen to vary by a factor of at least ~ 170 in damped Ly- α systems, where HI column densities are known (Curran et al. 2013). Clearly, extreme fluctuations of $T_{\text{s}}/C_{\text{f}}$ from source to source might also erase the $N_{\text{H}} - N_{\text{HI}}$ correlation. As in the case of T_{k} , the correlation we found excludes extreme fluctuations in $T_{\text{s}}/C_{\text{f}}$. Because T_{k} and T_{s} are related to each other, we can ultimately ascribe the correlation spread to fluctuations of $T_{\text{s}}/C_{\text{f}}$ about the assumed value.

To sum up, for a given source, the N_{HI} estimate from a spatially unresolved measurement of τ_{obs} must assume a value for the ratio $T_{\text{s}}/C_{\text{f}}$; typically, $T_{\text{s}}/C_{\text{f}}=100$ K is assumed. A different assumption about $T_{\text{s}}/C_{\text{f}}$ clearly leads to a different $N_{\text{H}} - N_{\text{HI}}$ offset. When we look for a correlation between X-ray and radio absorption in a sample of sources, we must also assume a $T_{\text{s}}/C_{\text{f}}$ ratio for each source. The simplest assumption is to assign the same ratio to all the sources. A posteriori, this assumption appears to be reasonable because we do find a correlation. However, this correlation shows a non-null spread, suggesting that each individual source might actually have a $T_{\text{s}}/C_{\text{f}}$ ratio slightly different from the value assumed for the entire sample. By estimating the spread, one can, in principle, estimate the fluctuations of the $T_{\text{s}}/C_{\text{f}}$ ratio of the individual sources about the value assumed for the en-

tire sample. As a proof of concept, we estimate the spread of the detection samples D' and D'' in Section 6.1.

6.1. Quantifying the spread of the $N_{\text{H}} - N_{\text{HI}}$ correlation

In order to simultaneously derive the correlation parameters of the $N_{\text{H}} - N_{\text{HI}}$ relation and quantify, for a given N_{H} , the intrinsic scatter of N_{HI} that might be due to the fluctuation of the ratio $T_{\text{s}}/C_{\text{f}}$ of the individual sources about a mean value, it is appropriate to resort to a Bayesian analysis. As a proof of concept, we performed a Bayesian analysis of the detection samples D' and D'' . We made use of the code APE-MoST¹⁵, which was developed by J. Buchner and M. Gruberbauer (Gruberbauer et al. 2009) and is suitable for non-censored data sets. A more sophisticated code, able to perform the Bayesian analysis on samples that include double-censored data (as our samples E' and E''), could be constructed based on the model developed by Kelly (2007); however, this implementation is beyond the scope of the present paper.

Although samples D' and D'' are biased, because they do not include non-detections, the results presented below are useful to illustrate how the intrinsic spread of the $N_{\text{H}} - N_{\text{HI}}$ relation can be quantified and interpreted. An additional advantage of the Bayesian analysis over the frequentist analysis is the possibility to take the uncertainties on both variables into account, even when the uncertainties are asymmetric.

Our data set is $DS=\{\log_{10}N_{\text{H}}^k, \log_{10}N_{\text{HI}}^k, \mathbf{S}^k\}$, where $\mathbf{S}^k = \{\sigma_+^k, \sigma_-^k, \epsilon_+^k, \epsilon_-^k\}$ is the vector of the upper and lower uncertainties on the k -th measures N_{H}^k and N_{HI}^k . The uncertainties on the N_{HI} values, for a given $T_{\text{s}}/C_{\text{f}}$, are available for two measurements only: the relative uncertainties are equal to 12% and 14%, respectively. Assuming that the remaining N_{HI} measurements are affected by comparable uncertainties, for the purpose of the Bayesian analysis only, to each of them we associated a conservative, relative uncertainty of 15%. Because the uncertainties on N_{HI} are much smaller than those on N_{H} , all the N_{HI} uncertainties have negligible effects on our results.

Given our data set DS , we determined the multi-dimensional probability density function (PDF) of the parameters $\theta = \{a, b, \sigma_{\text{int},\text{NHI}}\}$, where a and b are the parameters of the correlation (i.e., our model M):

$$\log_{10} N_{\text{HI}} = a + b \log_{10} N_{\text{H}} \pm \sigma_{\text{int},\text{NHI}}, \quad (5)$$

and $\sigma_{\text{int},\text{NHI}}$ is the intrinsic spread of the dependent variable.

In our analysis with APEMoST, we assumed independent flat priors for parameters a and b . For the internal dispersion $\sigma_{\text{int},\text{NHI}}$, which is a positive parameter, we assumed

$$p(\sigma_{\text{int},\text{NHI}}|M) = \frac{\mu^r}{\Gamma(r)} x^{r-1} \exp(-\mu x), \quad (6)$$

where $x = 1/\sigma_{\text{int},\text{NHI}}^2$, and $\Gamma(r)$ is the Euler gamma function. This PDF describes a variate with mean r/μ , and variance r/μ^2 . We set $r = \mu = 10^{-5}$ to assure an almost flat prior.

We used 2×10^6 MCMC iterations to guarantee a fairly complete sampling of the parameter space. The boundaries of the parameter space were set to $[-1000, 1000]$ for the a and b parameters, and to $[0.01, 1000]$ for the $\sigma_{\text{int},\text{NHI}}$ parameter.

¹⁵ Automated Parameter Estimation and Model Selection Toolkit; <http://apemost.sourceforge.net/>, 2011 February.

¹⁴ For the detection samples, we performed the regression analysis on a data set where N_{H} is the dependent variable (i.e., $\log_{10}N_{\text{H}} = A + B \log_{10}N_{\text{HI}}$), because the uncertainties are available for all the N_{H} measurements, whereas they are available for a minority of N_{HI} measurements only. Because the uncertainties on N_{HI} are typically smaller than those on N_{H} , the low significance of the linear fit also holds for the reverse relation.

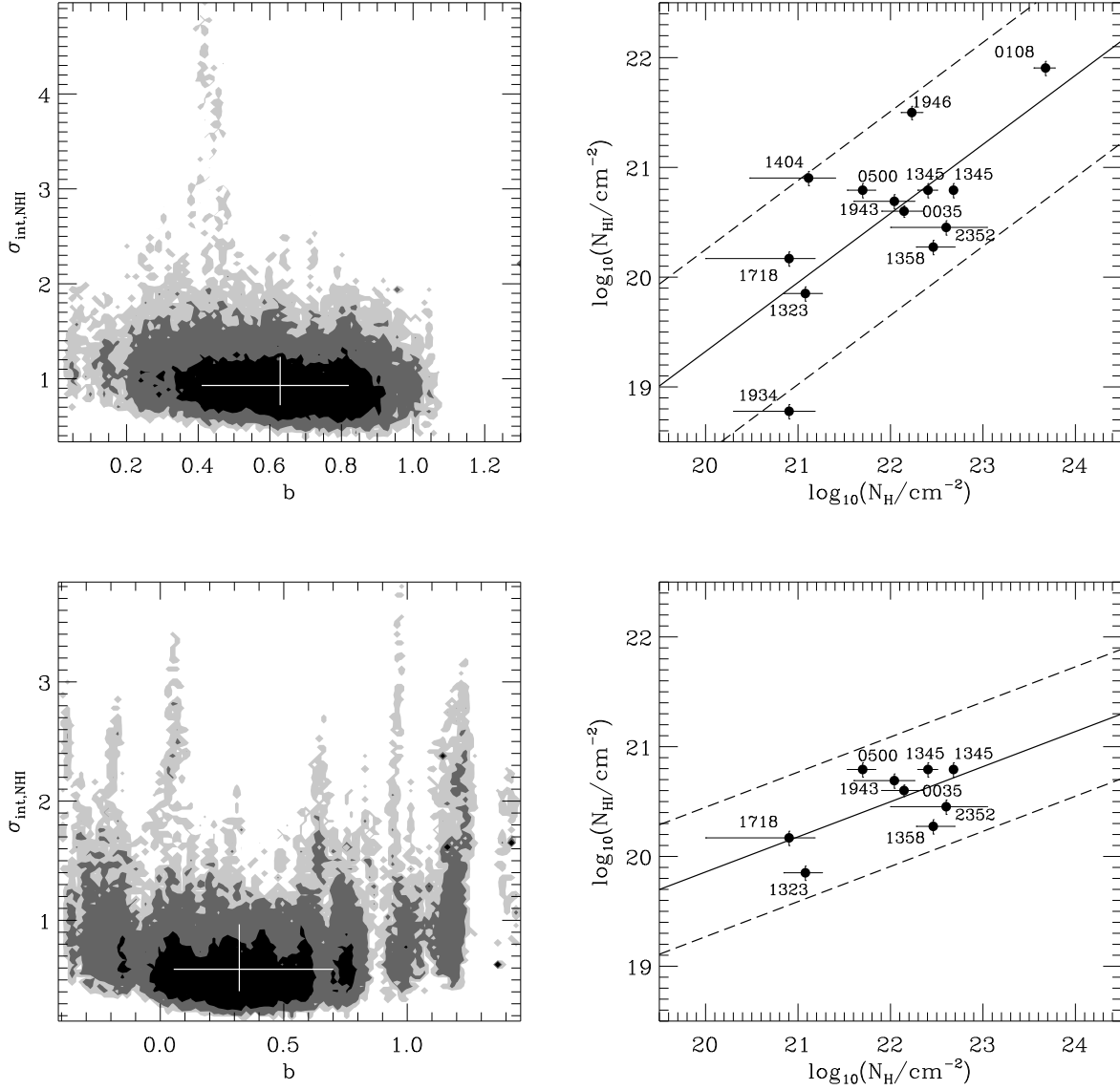


Figure 4. Bayesian analysis applied to sample D' (top) and D'' (bottom), with N_{H} as the independent variable and N_{HI} as dependent variable. The left panels show the marginalized PDFs of the parameters b and $\sigma_{\text{int},\text{NHI}}$. Black, gray, and light-gray shaded regions correspond to the 68.3, 95.4, and 99.7% confidence levels, respectively. The crosses show the median values and their marginalized 1σ uncertainty. The right panels show the $N_{\text{H}} - N_{\text{HI}}$ correlation: the solid symbols show the $(N_{\text{H}}, N_{\text{HI}})$ measurements with their 1σ error bars (relative uncertainties of 15% were assumed for the N_{HI} values whose uncertainty was not available in the literature; see text for details); the solid, straight line is the $N_{\text{H}} - N_{\text{HI}}$ relation $\log_{10} N_{\text{HI}} = a + b \log_{10} N_{\text{H}}$; the dashed lines show the $\pm\sigma_{\text{int},\text{NHI}}$ standard deviation of the relation; the parameters a , b , and $\sigma_{\text{int},\text{NHI}}$ are listed in Table 4.

The initial seed of the random number generator was set with the bash command `GSL_RANDOM_SEED=$RANDOM`.

The results of this analysis are reported in Table 4, and displayed in Figure 4.

Table 4
Bayesian Analysis of the Detection Samples, D' and D'' : Median Fit Parameters of the $N_{\text{H}} - N_{\text{HI}}$ Relation.

Sample	N_{data} (N_{sources})	a	b	$\sigma_{\text{int},\text{NHI}}$
D'	13 (12)	$6.7^{+4.8}_{-4.2}$	$0.63^{+0.19}_{-0.22}$	$0.92^{+0.30}_{-0.21}$
D''	9 (8)	$13.5^{+5.8}_{-8.4}$	$0.32^{+0.38}_{-0.27}$	$0.59^{+0.38}_{-0.18}$

Note. The uncertainties are the marginalized 68.3% confidence intervals.

Our analysis applied to sample D' shows that, for any given value of $\log_{10} N_{\text{H}}$, $\log_{10} N_{\text{HI}}$ takes the value $\log_{10} N_{\text{HI}} = a + b \log_{10} N_{\text{H}} \pm \sigma_{\text{int}, \text{NHI}}$ (with $a = 6.7_{-4.2}^{+4.8}$, $b = 0.63_{-0.22}^{+0.19}$, and $\sigma_{\text{int}, \text{NHI}} = 0.92_{-0.21}^{+0.30}$), with a 68% probability; this value of the intrinsic spread implies that, for any given N_{H} , the corresponding N_{HI} falls within a factor of $\simeq 8$ from the mean relation at the 68% confidence level.

As for the smaller sample D'' , our analysis yielded $b = 0.32_{-0.27}^{+0.38}$ and a smaller intrinsic spread, $\sigma_{\text{int}, \text{NHI}} = 0.59_{-0.18}^{+0.38}$, which implies that, for any given N_{H} , the corresponding N_{HI} falls within a factor of $\simeq 4$ from the mean relation with 68% probability. Because D'' was obtained from D' by removing the four ambiguous Compton-thin/thick sources, this means that those sources were responsible for the larger spread on N_{HI} that we found for sample D' (compare the top and bottom panels on the right-hand-side of Figure 4).

Overall, for the detection samples D' and D'' , the value of the regression line's slope is $b \simeq 0.3 - 0.6$, consistent with the results of the regression analyses presented in Section 5 for the estimate samples E' and E'' .

We discuss the possible implications of our exercise on the evaluation of the spread that might be due to $T_{\text{s}}/C_{\text{f}}$ fluctuations in Section 6.2.

6.2. Implications of the $N_{\text{H}} - N_{\text{HI}}$ correlation and its spread

The $N_{\text{H}} - N_{\text{HI}}$ correlation that we found in Section 5 suggests a physical connection between the X-ray and HI absorbers: the gas responsible for the X-ray obscuration and the HI absorption in compact radio galaxies may be part of the same, possibly unsettled, gaseous structure that extends over scales of a few hundred parsecs.

This scenario, also supported by recent X-ray and HI observations of a composite sample of compact radio sources (Glowacki et al. 2017), is corroborated by the X-ray absorption properties of the full X-ray emitting GPS/CSO sample: the mean total hydrogen column density of this sample (see Table 6) varies from $N_{\text{H}} \simeq (0.8 - 1) \times 10^{22} \text{ cm}^{-2}$ ($\sigma_{N_{\text{H}}} \simeq 0.2 - 0.3$ dex) to $N_{\text{H}} \simeq 3 \times 10^{22} \text{ cm}^{-2}$ ($\sigma_{N_{\text{H}}} \simeq 1$ dex), depending on whether absorbers that are not unambiguously Compton-thin are considered to be Compton-thin or Compton-thick sources, respectively. These values are consistent with a picture where the absorption of the X-rays from compact radio galaxies of the GPS/CSO type is comparable to the X-ray absorption in the extended FR-I and the unobscured FR-II radio galaxies. Together with the $N_{\text{H}} - N_{\text{HI}}$ correlation, which points toward a physical connection between the X-ray and radio absorbers, this evidence suggests that, in GPS/CSOs, the X-ray absorbing gas is located on scales larger than those of the parsec-scale, dusty tori typically invoked in AGN unification schemes. Such a scenario would imply that either “standard” dusty tori are not present in compact radio galaxies, or that the dominant contribution to the X-ray emission of GPS/CSOs does not originate in the accretion disc, but rather in the larger-scale jet/lobe components.

Even though the $N_{\text{H}} - N_{\text{HI}}$ correlation is statistically significant, the correlated data set is affected by a large intrinsic spread. For the detection samples, we could quantify the spread by means of a Bayesian analysis (Section 6.1). This spread could potentially provide us with interesting constraints on the properties of the neutral hydrogen in the ISM of the host galaxies of compact radio sources.

The $N_{\text{H}} - N_{\text{HI}}$ correlation that we found actually reflects

a correlation between N_{H} and τ_{obs} . Indeed, $N_{\text{HI}} \propto T_{\text{s}}/C_{\text{f}} \times \tau_{\text{obs}}$, with $\tau_{\text{obs}} \equiv \int \tau_{\text{obs}}(v) dv$ (see Equation (3)); in our case, the only observable is the velocity-integrated optical depth of the absorption line, τ_{obs} , because we only considered spatially unresolved observations ($C_{\text{f}} = 1$) and we assumed $T_{\text{s}} = 100$ K for the absorbing gas, so we obtained a ratio of $T_{\text{s}}/C_{\text{f}} = 100$ K for all the sources.

However, the ratio $T_{\text{s}}/C_{\text{f}}$ is seen to vary by a factor of at least ~ 170 (from 60 K to 9950 K) in damped Ly- α systems, where N_{HI} column densities are known (Curran et al. 2013); furthermore, the analysis of the compact quasar PKS 1549–79 suggests that $T_{\text{s}} > 3000$ K in this source (Holt et al. 2006); therefore, the assumption of a common value $T_{\text{s}}/C_{\text{f}} = 100$ K for the sources analyzed here is not well-justified.

If N_{H} and N_{HI} were intrinsically tightly correlated, the assumption of a constant $T_{\text{s}}/C_{\text{f}}$ would be responsible for the N_{HI} spread that we measured. As an example, when the intrinsic spread of N_{HI} is $\sigma_{\text{int}, \text{NHI}} = 0.92$ (as for sample D' , see Table 4), for any given N_{H} , the corresponding observed N_{HI} falls within a factor of $\simeq 8$ from the mean relation. However, if the correct value of N_{HI} actually lies on the mean relation, its observed deviation derives from the incorrect assumption $T_{\text{s}}/C_{\text{f}} = 100$ K and the factor of $\simeq 8$ has to be associated to the fluctuations of $T_{\text{s}}/C_{\text{f}}$ about 100 K; in other words, this ratio is expected to be in the range $T_{\text{s}}/C_{\text{f}} = 12 - 832$ K, at the 68% confidence level.

Therefore, we can, in principle, use our Bayesian result to forecast the true N_{HI} value and constrain the $T_{\text{s}}/C_{\text{f}}$ fluctuation: for any given N_{H} , the corresponding true N_{HI} value lies on the mean relation; by comparing the true value with the observed value, we can infer the deviation of the $T_{\text{s}}/C_{\text{f}}$ value from the assumed 100 K. This argument is sketched in Figure 5.

In our sample, the HI observations do not spatially resolve the source and the HI is observed only in absorption. Therefore, T_{s} and C_{f} cannot be disentangled, and the estimate of $T_{\text{s}}/C_{\text{f}}$ does not enable to constrain the spin temperature of the

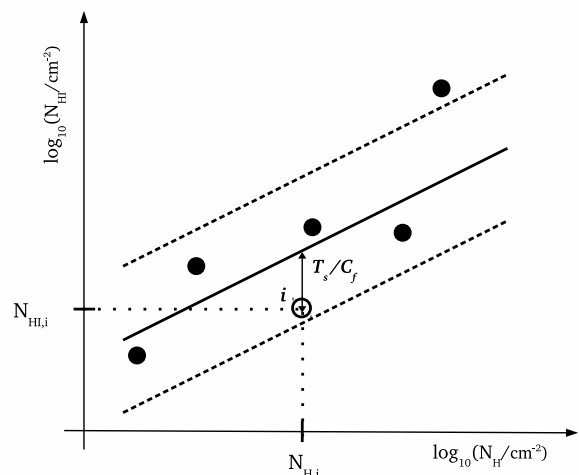


Figure 5. If a true $N_{\text{H}} - N_{\text{HI}}$ correlation exists (solid line), the observation of a source i off the correlation is due to a deviation of $T_{\text{s}}/C_{\text{f}}$ from the value assumed for the entire N_{HI} sample. Specifically, a source appears below the mean relation when the value of $T_{\text{s}}/C_{\text{f}}$ assumed for the sample is too low: the value of $T_{\text{s}}/C_{\text{f}}$ that is appropriate for source i and brings it back on the mean relation is proportionally larger, as indicated by the arrow.

gas. On the other hand, if HI measures of a sufficiently large sample of sources were based on high angular resolution observations, constraining T_{s} would, in principle, be possible. Indeed, this kind of observation enables to locate the HI absorber; the absorption profiles are derived only for the source region covered by the absorber, and the condition $C_{\text{f}} = 1$ is readily justified. Moreover, Equations (1) and (3) are more suitable for resolved observations; those equations hold under the assumption that the source is homogeneous, as appropriate when the source fraction considered for the evaluation of N_{HI} is small.

In conclusion, if a sample of resolved sources confirmed a correlation between N_{H} and N_{HI} , the deviation between the data-point of an individual source and the mean relation would return an estimate of the deviation of the spin temperature T_{s} of the HI in that source from the T_{s} assumed for the N_{HI} estimate of the entire sample.

7. CONCLUSIONS

We performed spatially unresolved HI absorption observations of a sample of X-ray emitting GPS/CSO galaxies with the WSRT, in order to improve the statistics of the $N_{\text{H}} - N_{\text{HI}}$ correlation sample and thoroughly investigate the possible connection between X-ray and radio absorbers in compact radio galaxies.

We confirmed the significant positive correlation between N_{H} and N_{HI} found by Ostorero et al. (2010), which implies that GPS/CSOs with increasingly large X-ray absorption have an increasingly larger probability of being detected in HI absorption observations. More interestingly, this correlation suggests that the gas responsible for the X-ray and radio absorption may be part of the same, possibly unsettled, hundred-parsec scale structure.

For the full, censored data set, the Akritas-Theil-Sen regression analysis yields $N_{\text{HI}} \propto N_{\text{H}}^b$, with $b = 0.47$ and $b = 0.35$, depending on the subsample. The correlation displays a large intrinsic spread, which may indicate that the $N_{\text{H}} - N_{\text{HI}}$ relation is not a one-to-one relation; additional variables are involved in the correlation and generate the intrinsic spread of the data set.

The estimate of N_{HI} relies on the assumed value of the ratio $T_{\text{s}}/C_{\text{f}}$ between the spin temperature of the absorbing gas and its covering factor. We suggested that the additional variable mostly responsible for the N_{HI} spread around the mean $N_{\text{H}} - N_{\text{HI}}$ correlation is the source-to-source fluctuation of $T_{\text{s}}/C_{\text{f}}$ with respect to the value assumed for the entire sample. An estimate of the N_{HI} spread at fixed N_{H} , i.e. $\sigma_{\text{int},N_{\text{HI}}}$, can be obtained through a Bayesian analysis. As a proof of concept, we performed this analysis on two uncensored subsamples only. For the larger subsample, we found $\sigma_{\text{int},N_{\text{HI}}} = 0.92$, implying that, for any given N_{H} , $T_{\text{s}}/C_{\text{f}}$ is expected to fall within a factor of $\simeq 8$, at the 68% confidence level, from the value $T_{\text{s}}/C_{\text{f}} = 100$ K assumed for the whole sample. If the existence of an $N_{\text{H}} - N_{\text{HI}}$ correlation were confirmed by high angular resolution observations of large enough samples, we could, in principle, disentangle T_{s} from C_{f} and constrain the deviation of the gas spin temperature, T_{s} , from the assumed value. This result would provide an unprecedented piece of information on the physical properties of the HI absorbing gas.

L.O. gratefully acknowledges support from the *Helena Kluyver* program run by ASTRON/JIVE. She is grateful to Ravi Sheth and to the Department of Physics and Astronomy of the University of Pennsylvania for support during the early stage of the project. She acknowledges funding from the University of Torino and Compagnia di San Paolo through the *Strategic Research Grant: Origin and Detection of Galactic and Extragalactic Cosmic Rays*. L.O. and A.D. acknowledge the INFN grant INDARK and the grant PRIN 2012 *Fisica Astroparticellare Teorica* of the Italian Ministry of University and Research. L.O., A.D., and A.L. are grateful to the Harvard-Smithsonian Center for Astrophysics for their kind hospitality. A.S. was supported by NASA through contract NAS8-03060 to the Chandra X-ray Center and NASA grants GO1-12145X, GO4-15099X. Ł.S. was supported by Polish NSC grant DEC-2012/04/A/ST9/00083. R.M. gratefully acknowledges support from the European Research Council under the European Union's Seventh Framework Programme (FP/2007-2013) /ERC Advanced Grant RADIOLIFE-320745. We are grateful to Gyula Józsa for his support during the observing runs with the WSRT and for providing us with the data-cubes of our target sources. We thank Johannes Buchner and Michael Gruberbauer for developing their superb code APEMoST and making it available to the community (apemost.sourceforge.net). Stefano Andreon is acknowledged for a very stimulating seminar on Bayesian statistics applied to astrophysics. We thank Guido Risaliti for stimulating discussions on AGN obscuration. We gratefully acknowledge an anonymous referee for a very careful revision of the paper and for constructive suggestions. The Westerbork Synthesis Radio Telescope is operated by the ASTRON (Netherlands Institute for Radio Astronomy) with support from the Netherlands Foundation for Scientific Research (NWO). This research has made use of the NASA/IPAC Extragalactic Database (NED), which is operated by the JPL, CalTech, under contract with NASA.

Facility: WSRT

Software: MIRIAD (Sault et al. 1995), ASURV (LaValley et al. 1992), APEMoST (Gruberbauer et al. 2009)

APPENDIX

All the N_{HI} and N_{H} estimates currently available for the 27 GPS/CSOs of the sample described in Section 4 are reported in Tables 5 and 6, respectively, together with the source properties that are most relevant to the present study. In these tables, the 22 sources of the correlation sample and the corresponding N_{HI} and N_{H} estimates that we used for the correlation analysis are highlighted with boldface fonts. The criteria that we adopted to select the above column density estimates among all the available estimates are described in Appendices A and B.

A. N_{HI} ESTIMATES

Table 5 lists the names of the 27 GPS/CSOs of the sample described in Section 4 (Column 1), their redshift (Column 2), their radio spectral and morphological classification as GPS and/or CSO (Column 3), their N_{HI} estimate (Column 4), the type (low/high-angular resolution) of HI absorption observation from which the N_{HI} estimate was derived, with possible

estimates of the covering factor of the absorbing gas (Column 5), the label associated with the absorption line(s) the N_{HI} estimate refers to (Column 6), the width of the absorption line (Column 7) and its peak optical depth (Column 8), the instrument used for the HI observation (Column 9), and the reference for the HI measurement (Column 10).

In this table, the 22 sources of the correlation sample and the corresponding N_{HI} estimates that we used for the correlation analysis are highlighted with boldface fonts. The criteria that we adopted to select the column density estimates highlighted in Column 4 among all the available estimates are described below.

For three sources of the correlation sample, both low angular resolution HI absorption measurements (unable to spatially resolve the source) and high angular resolution HI absorption measurements (able to spatially resolve the source) were available; in Table 5, Column 5, we denoted them by “U” (unresolved) and “R” (resolved), respectively. For self-consistency of the correlation analysis, we discarded the “R” measurements and made use of the “U” measurements only. For sources that were not detected, 3σ upper limits to N_{HI} were chosen for the analysis.

After applying these criteria, our sample of 22 sources turned out to be composed of two subsamples, in terms of

number of available N_{HI} estimates. For 10 out of 22 sources, only one unresolved N_{HI} estimate was available: we took this value for our correlation data set. Conversely, more than one unresolved N_{HI} estimate was available for any of the remaining 12 sources: for the purpose of our correlation analysis, we proceeded as follows.

For 5 out of 12 sources, two spectral features (marked with “I” and “II”, respectively, in Table 5, Column 6) were detected in the HI absorption spectra. In three of them, N_{HI} was available for each absorption line, but not for the full spectrum: we associated with each of these sources a value of N_{HI} estimated as the sum of the N_{HI} values of each spectral line (this is the value reported in Table 2). In the other two sources, besides the N_{HI} of each line, also the total N_{HI} (marked with “tot.” in Table 5, Column 6) was available: we associated the latter N_{HI} value with these sources.

For 7 out of 12 sources, either one or no absorption features were detected in different observations. When multiple N_{HI} values were available for a given source, we chose the most recent result. When an N_{HI} value and one or more *upper limits* to N_{HI} were available, we chose the N_{HI} value. When different 3σ *upper limits* to N_{HI} were available, we chose the most stringent one.

Table 5
HI Column Densities and Spectral Parameters.

Source Name	z_{opt}	GPS/CSO ^a	N_{HI} ($10^{20} \frac{T_s}{100\text{K}} \text{ cm}^{-2}$)	Res./Unres. (and C_f)	Line nr.	ΔV (km s^{-1})	τ_{peak} (10^{-2})	Instrument	References
B1950 (1)	(2)	(3)	(4)	(5)	(6)	(7)	(8)	(9)	(10)
0019–000	0.305	GPS	...	U	WSRT	P03
			$< 1.5^{\text{b,d}}$	U	$< 0.84^{\text{b}}$	WSRT	(*)
0026+346	0.517	GPS,CSO	WSRT	(*)
0035+227	0.096 ± 0.002	CSO	3.99 ± 0.49	U	...	114 ± 10	1.81 ± 0.14	WSRT	(*)
0108+388	0.66847	GPS,CSO	80.7	U	...	94 ± 10	44 ± 4	WSRT	C98
			80.5	U	...	100	43.7	WSRT	O06
0116+319	0.06	GPS,CSO	10.8	U	II	153 ± 6	3.7 ± 0.1	VLBA	v89
			12.2 ± 0.14	U	tot.	7.6, 153	3.0, 3.8	Arecibo	G06
0428+205	0.219	GPS,CSO	2.52	U	I	297	0.46	WSRT	V03
			0.93	U	II	247	0.21	WSRT	V03
0500+019	0.58457	GPS,CSO	6.2	U	tot.	~ 140	4	WSRT	C98
			2.5	U	I	45 ± 9	2.7 ± 0.3	WSRT	C98
			4.5	U	II	62 ± 7	3.6 ± 0.3	WSRT	C98
0710+439	0.518	GPS,CSO	...	U	WSRT	P03
			...	U	WSRT	(*)
0941–080	0.2281 ± 0.0013	GPS,CSO	$< 0.80^{\text{c}}$	U	< 0.44	WSRT	V03
			$< 1.26^{\text{b}}$	U	WSRT	P03
			0.91 ± 0.10	U	...	215 ± 18	0.22 ± 0.02	WSRT	(*)
1031+567	0.459	GPS,CSO	$< 0.87^{\text{c}}$	U	< 0.48	WSRT	V03
			$< 1.26^{\text{b}}$	U	WSRT	P03
			$< 1.8^{\text{b,d}}$	U	$< 0.99^{\text{b}}$	WSRT	(*)
1117+146	0.362	GPS,CSO	$< 0.38^{\text{c}}$	U	< 0.21	WSRT	V03
			$< 0.63^{\text{b}}$	U	WSRT	P03
			$< 1.1^{\text{b,d}}$	U	$< 0.62^{\text{b}}$	WSRT	(*)
1245+676	0.107	GPS,CSO	6.73	U	tot.	GMRT	S07
1323+321	0.370	GPS,CSO	0.71	U	...	229	0.17	WSRT	V03
1345+125	0.12174	GPS,CSO	6.2	U	tot.	150	1.38	Arecibo	M89
			~ 1.7	U	II	~ 2000	~ 0.15	WSRT	M03a
			~ 2	U	I	...	~ 1	WSRT	M03b
			~ 1	U	II	...	~ 0.2	WSRT	M03b
			~ 100	R (~ 0.2)	I	150	$\gtrsim 60$	VLBI	M04
			440 ^f	R	I	...	60	VLBI	M13
			46	R	II	VLBI	M13
1358+624	0.431	GPS,CSO	1.88	U	...	170	0.61	WSRT	V03
1404+286	0.07658	GPS,CSO	1.83	U	...	256	0.39	WSRT	V03
	0.0773		8.0	U	...	1800	0.5	WSRT	O06
1509+054	0.084	GPS,CSO	< 3.64	U	< 0.02	WSRT	P03
1607+268	0.473	GPS,CSO	...	U	WSRT	P03
			$< 1.6^{\text{b,d}}$	U	$< 0.86^{\text{b}}$	WSRT	(*)
1718–649	0.0142	GPS,CSO	0.703	U	I	43(FWZI)	0.4	ATCA	M14

Table 5 — *Continued*

Source Name	z_{opt}	GPS/CSO ^a	N_{HI} ($10^{20} \frac{T_s}{100 \text{ K}} \text{ cm}^{-2}$)	Res./Unres. (and C_f)	Line nr.	ΔV (km s^{-1})	τ_{peak} (10^{-2})	Instrument	References
(1)	(2)	(3)	(4)	(5)	(6)	(7)	(8)	(9)	(10)
1843+356	0.764	GPS,CSO	0.774 < 6.92 ^c < 10.4 ^{b,d} < 11.7 ^{b,d}	U U U U	II	65(FWZI)	0.2 < 3.80 < 5.70 ^b < 6.41 ^b	ATCA WSRT WSRT WSRT	M14 V03 V03 ^e (*)
1934–638	0.18129	GPS,CSO	0.06	U	...	100	0.22	ATCA, LBA	V00
1943+546	0.263	GPS,CSO	4.91	U	tot.	315	0.86	WSRT	V03
1946+708	0.101	GPS,CSO	31.6 [2.5 – 27.33] ^f	U R(~ 1)	tot. I-tot.	357 [40.1 – 357]	5.00 \pm 0.7 [3.3 – 7.0]	VLA VLBA	P03,P99 P99
2008–068	0.547	GPS,CSO	...	U	WSRT	(*)
2021+614	0.227	GPS,CSO	< 0.24 ^c < 0.398 ^b < 0.27 ^{b,d}	U U U	< 0.13 ... < 0.15 ^b	WSRT WSRT WSRT	V03 P03 (*)
2128+048	0.99	GPS,CSO	< 2.08 ^{b,d}	U	< 1.14 ^b	WSRT	(*)
2352+495	0.2379	GPS,CSO	0.28 2.56 0.91 \pm 0.13 ^f 6.5 \pm 0.3 ^{f,†}	U U R(~ 0.2) R(~ 0.2)	I II I II	13 82 13 \pm 2 85 \pm 4	1.16 1.72	WSRT WSRT VLBA VLBA	V03 V03 A10 A10

References. — (*): this work; A10: Araya et al. (2010); C98: Carilli et al. (1998); G06: Gupta et al. (2006); M14: Maccagni et al. (2014); M89: Mirabel (1989); M04: Morganti et al. (2004); M13: Morganti et al. (2013); O06: Orienti et al. (2006); P03: Pihlström et al. (2003); P99: Peck et al. (1999); S07: Saikia et al. (2007); v89: van Gorkom et al. (1989); V00: Véron-Cetty et al. (2000); V03: Vermeulen et al. (2003).

Note. The N_{HI} values in boldface fonts are those used for the correlation analysis described in Section 5. When two spectral lines are detected, the corresponding N_{HI} are labelled as I (narrower line) and II (broader line).

^a References for GPS classification: de Vries et al. (1997), Tingay et al. (1997), Snellen et al. (1998), Stanghellini et al. (1998), Toriainen et al. (2007), and Vermeulen et al. (2003); references for CSO classification: Augusto et al. (2006), Bondi et al. (2004), Dallacasa et al. (1998), Nagai et al. (2006), Orienti et al. (2006), Polatidis & Conway (2003), Stanghellini et al. (1997), Stanghellini et al. (1999), and Stanghellini et al. (2001).

^b 3σ upper limit.

^c 2σ upper limit, derived by V03 from the relation: $N_{\text{HI},2\sigma} = 1.82 \times 10^{18} \times T_s \times \tau_{\text{obs},2\sigma} \times \Delta V$, under the assumption $T_s=100 \text{ K}$, $\Delta V = 100 \text{ km s}^{-1}$, and $C_f = 1$.

^d From results on $\tau_{\text{obs},3\sigma}$, using the relation: $N_{\text{HI},3\sigma} = 1.823 \times 10^{18} \times T_s \times \tau_{\text{obs},3\sigma} \times \Delta V$, under the assumptions $T_s=100 \text{ K}$, $\Delta V = 100 \text{ km s}^{-1}$, and $C_f = 1$.

^e From the 2σ estimates by V03, we derived the 3σ estimates reported in this row.

^f N_{HI} values rescaled to $T_s = 100 \text{ K}$ (A10 and P99 assumed $T_s = 8000 \text{ K}$).

[†] This value of N_{HI} was chosen for the T_s estimate discussed in Section 6.2.

B. N_{H} ESTIMATES

Table 6 lists the names of the 27 GPS/CSOs of the sample described in Section 4 (Column 1), their redshift (Column 2), the Galactic column density, $N_{\text{H,Gal}}$, toward the source (Column 3), the local (i.e., source-intrinsic) absorbing column density, N_{H} , derived from the X-ray spectrum (Column 4), the X-ray photon spectral index (Column 5), and the reference for the X-ray data (Column 6).

In this table, the 22 sources of the correlation sample and the corresponding N_{H} estimates that we used for the correlation analysis are highlighted with boldface fonts. The criteria that we adopted to select the column density estimates highlighted in Column 4 among all the available estimates are described below.

We took the N_{H} estimates from the literature. These estimates were derived from the X-ray spectra with different methods. When the signal-to-noise ratio was good enough to perform a spectral analysis, N_{H} was derived by fitting a

model spectrum, absorbed by both the Galactic and a local (i.e., at redshift z_{opt}) gas column density, to the observed X-ray spectrum. In the fitting procedure, the Galactic column density parameter, $N_{\text{H,Gal}}$, was always fixed, whereas the local column density parameter, N_{H} , and the photon spectral index parameter, Γ , were left free to vary. On the other hand, when the signal-to-noise ratio was too low to enable a standard spectral analysis, in some cases (e.g., Vink et al. 2006; Siemiginowska et al. 2016), N_{H} was constrained by performing the above spectral fitting, but with Γ frozen to a value (or to a range of values) typical for radio galaxies. In other cases (e.g., Tengstrand et al. 2009), N_{H} constraints were derived with a technique based on a comparison of the observed and simulated hardness ratios of the X-ray spectra.

All the available N_{H} estimates, in the form of either values with corresponding 1σ uncertainties, upper limits, or lower limits, are reported in Table 6, Column 4. The remaining parameters of the X-ray spectral fitting, $N_{\text{H,Gal}}$ and Γ , are reported in Columns 3 and 5 of the same Table, respectively.

For some of the sources, different estimates of N_{H} were derived from the analysis of X-ray observations carried out at different epochs and/or with different detectors, as well as from the analysis of the same X-ray data set either by different authors or with different techniques. Furthermore, the X-ray spectra of some sources could be satisfactorily fit with different models, implying different absorption estimates.

In all the cases in which we had multiple choices for the N_{H} estimate, we adopted the following criteria for the purpose of our correlation analysis, unless otherwise stated. We discarded the values derived from soft X-ray data only (e.g., ROSAT data). When more recent X-ray data of a given source proved that the older results were affected by poor angular resolution, we chose the most accurate (also the most recent) value when the two values were consistent with each other at the 1σ level, whereas we took both values into account when they were not consistent with each other, in that we could not rule out long-term column-density variations. When two different data sets yielded different N_{H} upper limits, we chose the less stringent one.¹⁶ When the same data set was analyzed

¹⁶ We note that this choice differs from the choice taken for N_{HI} upper

by different authors with the same model, we chose the result of the most recent analysis. When the same data set was analyzed by the same authors with the same model, but with different techniques, we chose the result of the most robust analysis (e.g., we discarded an N_{H} value derived by fixing the spectral index Γ in favor of an upper or lower limit to N_{H} derived without any constraints on Γ). When more than one model spectrum could be satisfactorily fit to a given observed spectrum, we selected the N_{H} estimate derived from the simplest model among those that include a Compton-thin absorber. When a Compton-thick absorber scenario could also apply to the source, we always took into account also the N_{H} lower limit ($N_{\text{H}} \gtrsim 10^{24} \text{ cm}^{-2}$) derived in the framework of this scenario. The latter case applied to a subsample of

limits at the end of Section 4.1: when we have upper limits, we choose the most and the least stringent limit for N_{HI} and N_{H} , respectively. This choice is motivated by the fact that N_{HI} upper limits are derived from the continuum flux density and the rms noise level of the radio spectra, whereas N_{H} upper limits are derived from the likelihood function of the parametric fit to the X-ray spectra. Therefore, in the N_{HI} case, the most stringent upper limit

three sources. Finally, when a *lower* limit to N_{H} was derived in a Compton-thin scenario,¹⁷ we could not state whether the source was Compton-thin or Compton-thick; we thus considered both scenarios to be plausible, as in the previous case. In the Compton-thin scenario, we associated with the source an N_{H} value equal to the mean of the 3σ lower limit and the physical upper bound of the Compton-thin N_{H} range (i.e., $N_{\text{H}} \simeq 10^{24} \text{ cm}^{-2}$). We considered the N_{H} range as a $\pm 3\sigma$ interval, and thus associated with the mean N_{H} the corresponding 1σ uncertainty. Overall, the ambiguity between a Compton-thin and a Compton-thick absorber (and between the corresponding values of N_{H}) affected a subsample of four sources of the correlation sample.

corresponds to data affected by the lowest noise, whereas in the N_{H} case, the quality of the data of different observations is comparable and the least stringent upper limit represents the most conservative choice.

¹⁷ This case applies to one source only, i.e. 0108+388.

Table 6
X-ray Column Densities and Spectral Parameters.

Source Name B1950 (1)	z_{opt} (2)	$N_{\text{H,Gal}}$ (10^{20} cm^{-2}) (3)	N_{H} (10^{22} cm^{-2}) (4)	Γ (5)	References (6)
0019–000	0.305	2.7	< 100	...	T09
0026+346	0.517	5.6	$1.0^{+0.5}_{-0.4}$	$1.43^{+0.20}_{-0.19}$	G06
0035+227	0.096 ± 0.002	3.37	$1.4^{+0.8}_{-0.6}$	$1.7^{\text{a,b}}$	S16
0108+388	0.66847	5.8	57 ± 20	1.75^{a}	V06
		5.8	> 18^{c}	...	V06
			> 5	...	T09
0116+319	0.06	5.67	S16
0428+205	0.219	19.6	< 0.69^d	$[0.63 - 2.62]^{\text{a}}$	T09
0500+019	0.58457	8.3	$0.5^{+0.3}_{-0.2}$	$1.62^{+0.21}_{-0.19}$	G06
		...	$0.5^{+0.18}_{-0.16}$	$1.61^{+0.16}_{-0.15}$	T09
0710+439	0.518	8.11	0.44 ± 0.08	1.59 ± 0.06	V06
			$0.51^{+0.17}_{-0.14}$	1.59 ± 0.06	T09
		8.0	0.58 ± 0.08	1.59 ± 0.07	S16
		8.0	$0.61^{+0.04}_{-0.08}$	$1.64^{+0.09}_{-0.07}$	S16
		8.0	$0.49^{+0.07}_{-0.06}$...	S16
		8.0	0.58 ± 0.08	$1.42^{+0.14}_{-0.20}$	S16
		8.0	0.56 ± 0.08	$1.39^{+0.17}_{-0.23}$	S16
		8.0	$1.02^{+0.29}_{-0.22}$	$1.75^{+0.11}_{-0.10}$	S16
0941–080	0.2281 ± 0.0013	3.7	...	2^{a}	G06
		3.67	...	$2.62^{+1.29}_{-1.03}$	S08
		3.67	< 1.26^c	$2.28^{+0.67}_{-0.61}$	S08, O10
		3.67	< 0.53^{c}	$[1.7 - 1.9]^{\text{a}}$	S08, O10
		3.67	< 100	...	T09
1031+567	0.45	0.56	0.50 ± 0.18	1.75^{a}	V06
		...	0.50 ± 0.18	...	T09
1117+146	0.362	2.0	< 0.16^d	$[0.63 - 2.62]^{\text{a}}$	T09
1245+676	0.107	S16, W09
1323+321	0.370	1.2	$0.12^{+0.06}_{-0.05}$	1.7 ± 0.2	T09
1345+125	0.12174	1.1	$4.2^{+4.0}_{-2.4}$	$1.6^{+1.2}_{-0.8}$	O00
		...	4.8 ± 0.4	$1.1^{+0.7}_{-0.8}$	T09
		1.9	$2.543^{+0.636}_{-0.580}$	$1.10^{+0.29}_{-0.28}$	S08
		1.9	$2.28^{+0.36}_{-0.35}$	$1.27^{+0.21}_{-0.19}$	S08
1358+624	0.431	1.96	3.0 ± 0.7	1.24 ± 0.17	V06
		...	2.9^{+2}_{-1}	1.24 ± 0.17	T09
1404+286	0.07658	1.4	$0.13^{+0.12}_{-0.10}$	$2.1^{+0.6}_{-0.3}$, $0.7^{+0.3}_{-0.4}$	G04
		1.4	$0.12^{+0.09}_{-0.08}$, $24.0^{+10.0}_{-8.0}$	$2.0^{+0.4}_{-0.3}$	G04
		1.4	$0.11 \pm 0.05^{\text{e}}$, > 90^{f,g}	$2.21^{+0.19}_{-0.14}$	G04
		1.4	$0.19^{+0.13}_{-0.10}$, > $90^{\text{f,g}}$	$2.6 \pm 0.5^{\text{e}}$, $2^{\text{a,f}}$	G04
		1.4	$0.09^{+0.08}_{-0.06}$, > $90^{\text{f,g}}$	$2.2 \pm 0.4^{\text{h}}$	G04

Table 6 — *Continued*

Source Name B1950 (1)	z_{opt} (2)	$N_{\text{H,Gal}}$ (10^{20} cm^{-2}) (3)	N_{H} (10^{22} cm^{-2}) (4)	Γ (5)	References (6)
		1.4	$< 0.08^{\text{e}}, > 90^{\text{f,g}}$	$1.2^{+2.0}_{-0.3}$	G04
		...	$0.08^{+0.31}_{-0.05}$	$2.4^{+2.1}_{-1.1}$	G04
		...	> 90	$2.21^{+0.19}_{-0.14}$	T09
1509+054	0.084	3.29	< 0.23	1.0 ± 0.2	S16, K09
1607+268	0.473	3.8	< 0.2	0.4 ± 0.3	T09
		3.8	> 60	...	T09
		4.1	< 0.18	1.4 ± 0.1	S16
1718-649	0.0142	7.15	0.08 ± 0.07	1.6 ± 0.2	S16
1843+356	0.764	6.75	$0.8^{+0.9}_{-0.7}$	$1.7^{\text{a,b}}$	S16
1934-638	0.18129	...	> 250	$1.9^{+0.5}_{-0.6}$	R03
		...	< 2.0	...	R03
		6.16	$0.08^{+0.07}_{-0.06}$	$1.67^{+0.15}_{-0.16}$	S16
1943+546	0.263	13.15	1.1 ± 0.7	$1.7^{\text{a,b}}$	S16
1946+708	0.101	...	$2.60^{+2.5}_{-1.90}$	$2.6^{+0.6}_{-0.7}$	R03
		...	> 280	...	R03
		8.57	$1.7^{+0.5}_{-0.4}$	1.7 ± 0.4	S16
2008-068	0.547	5.0	$< 0.48^{\text{d}}$	$[0.63 - 2.62]^{\text{a}}$	T09
2021+614	0.227	14.01	< 1.02	$0.8^{+0.3}_{-0.2}$	S16
2128+048	0.99	5.2	$0.3^{+0.81}_{-0.3}$	$1.5^{+0.6}_{-0.7}$	G06
		5.2	...	$1.28^{+0.42}_{-0.41}$	S08
		5.2	< 1.56	$1.44^{+0.89}_{-0.70}$	S08, O10
		5.0	< 1.9	$1.98^{+0.5}_{-0.4}$	T09
2352+495	0.2379	12.4	0.66 ± 0.27	1.75^{a}	V06
		...	4^{+7}_{-3}	$1.8^{+1.6}_{-0.9}$	T09

References. — G04: Guainazzi et al. (2004); G06: Guainazzi et al. (2006); K09: Kuraszkiewicz et al. (2009); O00: O’Dea et al. (2000); O10: Ostorero et al. (2010); R03: Risaliti et al. (2003); S08: Siemiginowska et al. (2008); S16: Siemiginowska et al. (2016); T09: Tengstrand et al. (2009); V06: Vink et al. (2006); W09: Watson et al. (2009).

Note. The values of N_{H} in boldface fonts are those used for the correlation analysis in Section 5.

^a Fixed.

^b By varying Γ in the range [1.4-2.0], the authors get N_{H} values consistent, to within 1σ , with the N_{H} value given in this Table.

^c 3σ (upper or lower) limit.

^d Upper bound of the 1.6σ interval [N_{Hmin} , N_{Hmax}] about the curve corresponding to the nominal hardness ratio, when Γ is constrained to the given range.

^e Soft X-rays.

^f Hard X-rays.

^g $N_{\text{H}}^{\text{hard}} > 9 \times 10^{23} \text{ cm}^{-2}$ is associated with a Compton-reflection model for the hard X-rays.

^h Intrinsic, for the Compton-reflection model.

REFERENCES

- Akritas, M. G., Murphy, S. A., & LaValley, M. P. 1995, *JASA*, 90, 170
 Alexander, P. 2000, *MNRAS*, 319, 8
 Allison, J. R., Curran, S. J., Emonts, B. H. C., et al. 2012, *MNRAS*, 423, 2601
 Antonucci, R. 1993, *ARA&A*, 31, 473
 Araya, E. D., Rodríguez, C., Pihlström, Y., et al. 2010, *AJ*, 139, 17
 Augusto, P., Gonzalez-Serrano, J. I., Perez-Fournon, I., & Wilkinson, P. N. 2006, *MNRAS*, 368, 1411
 Bahcall, J. N., & Ekers, R. D. 1969, *ApJ*, 157, 1055
 Bondi, M., Marchà, M. J. M., Polatidis, A., et al. 2004, *MNRAS*, 352, 112
 Carilli, C. L., Menten, K. M., Reid, M. J., Rupen, M. P., & Yun, M. S. 1998, *ApJ*, 494, 175
 Chandola, Y., Sirothia, S. K., & Saikia, D. J. 2011, *MNRAS*, 418, 1787
 Chiaberge, M., Capetti, A., & Celotti, A. 1999, *A&A*, 349, 77
 —. 2000, *A&A*, 355, 873
 Conway, J. 1997, in *Gigahertz Peaked Spectrum and Compact Steep Spectrum Radio Sources*, ed. I. A. G. Snellen, R. T. Schilizzi, H. J. A. Roettgering, & M. N. Bremer, 198–207
 Conway, J. E. 1999, *New A Rev.*, 43, 509
 Curran, S. J., Allison, J. R., Glowacki, M., Whiting, M. T., & Sadler, E. M. 2013, *MNRAS*, 431, 3408
 Curran, S. J., & Whiting, M. T. 2010, *ApJ*, 712, 303
 Curran, S. J., Whiting, M. T., Wiklind, T., et al. 2008, *MNRAS*, 391, 765
 Czerny, B., Siemiginowska, A., Janiuk, A., Nikiel-Wroczyński, B., & Stawarz, L. 2009, *ApJ*, 698, 840
 Dallacasa, D., Bondi, M., Alef, W., & Mantovani, F. 1998, *A&AS*, 129, 219
 de Vries, W. H., Barthel, P. D., & O’Dea, C. P. 1997, *A&A*, 321, 105
 de Vries, W. H., O’Dea, C. P., Barthel, P. D., & Thompson, D. J. 2000, *A&AS*, 143, 181
 Donato, D., Sambruna, R. M., & Gliozzi, M. 2004, *ApJ*, 617, 915
 Dunlop, J. S., Peacock, J. A., Savage, A., et al. 1989, *MNRAS*, 238, 1171
 Emonts, B. H. C., Burnett, C., Morganti, R., & Struve, C. 2012, *MNRAS*, 421, 1421
 Fanti, C., Fanti, R., Dallacasa, D., et al. 1995, *A&A*, 302, 317
 Feigelson, E. D., & Babu, G. J. 2012, *Modern Statistical Methods for Astronomy*
 Gallimore, J. F., Baum, S. A., O’Dea, C. P., Pedlar, A., & Brinks, E. 1999, *ApJ*, 524, 684
 Geréb, K., Maccagni, F. M., Morganti, R., & Oosterloo, T. A. 2015, *A&A*, 575, A44
 Geréb, K., Morganti, R., & Oosterloo, T. A. 2014, *A&A*, 569, A35
 Glowacki, M., Allison, J. R., Sadler, E. M., et al. 2017, *MNRAS*, 467, 2766
 Gruberbauer, M., Kallinger, T., Weiss, W. W., & Guenther, D. B. 2009, *A&A*, 506, 1043
 Guainazzi, M., Siemiginowska, A., Rodriguez-Pascual, P., & Stanghellini, C. 2004, *A&A*, 421, 461
 Guainazzi, M., Siemiginowska, A., Stanghellini, C., et al. 2006, *A&A*, 446, 87
 Gupta, N., Salter, C. J., Saikia, D. J., Ghosh, T., & Jeyakumar, S. 2006, *MNRAS*, 373, 972
 Heinz, S., Reynolds, C. S., & Begelman, M. C. 1998, *ApJ*, 501, 126
 Holt, J., Tadhunter, C., Morganti, R., et al. 2006, *MNRAS*, 370, 1633
 Isobe, T., Feigelson, E. D., & Nelson, P. I. 1986, *ApJ*, 306, 490

- Jaffe, W., Meisenheimer, K., Röttgering, H. J. A., et al. 2004, *Nature*, 429, 47
- Kelly, B. C. 2007, *ApJ*, 665, 1489
- Krolik, J. H., & Begelman, M. C. 1988, *ApJ*, 329, 702
- Kuraszkiewicz, J., Wilkes, B. J., Schmidt, G., et al. 2009, *ApJ*, 692, 1143
- LaValley, M. P., Isobe, T., & Feigelson, E. D. 1992, in *Bulletin of the American Astronomical Society*, Vol. 24, *Bulletin of the American Astronomical Society*, 839–840
- Liszt, H. 2001, *A&A*, 371, 698
- Maccagni, F. M., Morganti, R., Oosterloo, T. A., & Mahony, E. K. 2014, *A&A*, 571, A67
- Maloney, P. R., Hollenbach, D. J., & Tielens, A. G. G. M. 1996, *ApJ*, 466, 561
- Marcha, M. J. M., Browne, I. W. A., Impey, C. D., & Smith, P. S. 1996, *MNRAS*, 281, 425
- Migliori, G., Siemiginowska, A., Sobolewska, M., et al. 2016, *ApJL*, 821, L31
- Mirabel, I. F. 1989, *ApJL*, 340, L13
- Morganti, R., Fogasy, J., Paragi, Z., Oosterloo, T., & Orienti, M. 2013, *Science*, 341, 1082
- Morganti, R., Oosterloo, T., Struve, C., & Saripalli, L. 2008, *A&A*, 485, L5
- Morganti, R., Oosterloo, T. A., Tadhunter, C. N., et al. 2001, *MNRAS*, 323, 331
- . 2004, *A&A*, 424, 119
- Morganti, R., Tadhunter, C. N., Oosterloo, T. A., et al. 2003, *PASA*, 20, 129
- Nagai, H., Inoue, M., Asada, K., Kameno, S., & Doi, A. 2006, *ApJ*, 648, 148
- Nenkova, M., Sirocky, M. M., Nikutta, R., Ivezić, Ž., & Elitzur, M. 2008, *ApJ*, 685, 160
- O’Dea, C. P., Baum, S. A., & Gallimore, J. F. 1994, *ApJ*, 436, 669
- O’Dea, C. P., De Vries, W. H., Worrall, D. M., Baum, S. A., & Koekemoer, A. 2000, *AJ*, 119, 478
- Orienti, M., Morganti, R., & Dallacasa, D. 2006, *A&A*, 457, 531
- Ostorero, L., Moderski, R., Stawarz, L., et al. 2009, *Astronomische Nachrichten*, 330, 275
- Ostorero, L., Morganti, R., Diaferio, A., et al. 2016, *Astronomische Nachrichten*, 337, 148
- Ostorero, L., Moderski, R., Stawarz, L., et al. 2010, *ApJ*, 715, 1071
- Pearson, T. J., & Readhead, A. C. S. 1988, *ApJ*, 328, 114
- Peck, A. B., & Taylor, G. B. 2001, *ApJL*, 554, L147
- Peck, A. B., Taylor, G. B., & Conway, J. E. 1999, *ApJ*, 521, 103
- Perlman, E. S., Stocke, J. T., Carilli, C. L., et al. 2002, *AJ*, 124, 2401
- Perucho, M. 2016, *Astronomische Nachrichten*, 337, 18
- Pihlström, Y. M., Conway, J. E., & Vermeulen, R. C. 2003, *A&A*, 404, 871
- Polatidis, A. G., & Conway, J. E. 2003, *PASA*, 20, 69
- Raban, D., Jaffe, W., Röttgering, H., Meisenheimer, K., & Tristram, K. R. W. 2009, *MNRAS*, 394, 1325
- Readhead, A. C. S., Taylor, G. B., Pearson, T. J., & Wilkinson, P. N. 1996, *ApJ*, 460, 634
- Reynolds, C. S., & Begelman, M. C. 1997, *ApJL*, 487, L135
- Ride, S. K., & Walker, Jr., A. B. C. 1977, *A&A*, 61, 339
- Risaliti, G., Elvis, M., Bianchi, S., & Matt, G. 2010, *MNRAS*, 406, L20
- Risaliti, G., Elvis, M., Fabbiano, G., et al. 2007, *ApJL*, 659, L111
- Risaliti, G., Nardini, E., Salvati, M., et al. 2011, *MNRAS*, 410, 1027
- Risaliti, G., Woltjer, L., & Salvati, M. 2003, *A&A*, 401, 895
- Saikia, D. J., Gupta, N., & Konar, C. 2007, *MNRAS*, 375, L31
- Sambruna, R. M., Eracleous, M., & Mushotzky, R. F. 1999, *ApJ*, 526, 60
- Sault, R. J., Teuben, P. J., & Wright, M. C. H. 1995, in *Astronomical Society of the Pacific Conference Series*, Vol. 77, *Astronomical Data Analysis Software and Systems IV*, ed. R. A. Shaw, H. E. Payne, & J. J. E. Hayes, 433
- Siemiginowska, A. 2009, *Astronomische Nachrichten*, 330, 264
- Siemiginowska, A., LaMassa, S., Aldcroft, T. L., Bechtold, J., & Elvis, M. 2008, *ApJ*, 684, 811
- Siemiginowska, A., Sobolewska, M., Migliori, G., et al. 2016, *ApJ*, 823, 57
- Snellen, I. A. G., Schilizzi, R. T., de Bruyn, A. G., et al. 1998, *A&AS*, 131, 435
- Snellen, I. A. G., Schilizzi, R. T., Miley, G. K., et al. 2000, *MNRAS*, 319, 445
- Stanghellini, C., Dallacasa, D., O’Dea, C. P., et al. 2001, *A&A*, 377, 377
- Stanghellini, C., O’Dea, C. P., Baum, S. A., et al. 1997, *A&A*, 325, 943
- Stanghellini, C., O’Dea, C. P., Dallacasa, D., et al. 1998, *A&AS*, 131, 303
- Stanghellini, C., O’Dea, C. P., & Murphy, D. W. 1999, *A&AS*, 134, 309
- Stawarz, L., Ostorero, L., Begelman, M. C., et al. 2008, *ApJ*, 680, 911
- Struve, C., & Conway, J. E. 2010, *A&A*, 513, A10
- Tadhunter, C. 2008, *New A Rev.*, 52, 227
- Taylor, G. B., Readhead, A. C. S., & Pearson, T. J. 1996, *ApJ*, 463, 95
- Tengstrand, O., Guainazzi, M., Siemiginowska, A., et al. 2009, *A&A*, 501, 89
- Tingay, S. J., Jauncey, D. L., Reynolds, J. E., et al. 1997, *AJ*, 113, 2025
- Tornainen, I., Tornikoski, M., Lähteenmäki, A., et al. 2007, *A&A*, 469, 451
- Tristram, K. R. W., Burtscher, L., Jaffe, W., et al. 2014, *A&A*, 563, A82
- Tristram, K. R. W., Raban, D., Meisenheimer, K., et al. 2009, *A&A*, 502, 67
- Urry, C. M., & Padovani, P. 1995, *PASP*, 107, 803
- van Gorkom, J. H., Knapp, G. R., Ekers, R. D., et al. 1989, *AJ*, 97, 708
- Vermeulen, R. C., Pihlström, Y. M., Tschager, W., et al. 2003, *A&A*, 404, 861
- Véron-Cetty, M.-P., Woltjer, L., Staveley-Smith, L., & Ekers, R. D. 2000, *A&A*, 362, 426
- Vink, J., Snellen, I., Mack, K.-H., & Schilizzi, R. 2006, *MNRAS*, 367, 928
- Wagner, A. Y., Bicknell, G. V., & Umemura, M. 2012, *ApJ*, 757, 136
- Watson, M. G., Schröder, A. C., Fyfe, D., et al. 2009, *A&A*, 493, 339
- Wilms, J., Allen, A., & McCray, R. 2000, *ApJ*, 542, 914
- Wolfe, A. M., & Burbidge, G. R. 1975, *ApJ*, 200, 548